Investigation of Magnons in Rare Earth Metals by Inelastic Neutron Scattering

Bjerrum Møller, H.

Publication date:
1968

Document Version
Publisher's PDF, also known as Version of record

Investigation of Magnons in Rare Earth Metals by Inelastic Neutron Scattering

by

H. Bjerrum Møller

BLANK

PAGE

Risö Report No. 178

Investigation of Magnons in Rare Earth Metals by Inelastic Neutron Scattering

by

H. Bjerrum Møller

Danish Atomic Energy Commission
Research Establishment Risö
Roskilde. 1968

Denne afhandling er af det matematisk-naturvidenskabelige fakultet ved Københavns Universitet antaget til offentlig at forsvares for den filosofiske doktorgrad.

København, den 8. april 1968.

MORTEN LANGE
h. a. dec.

Contents

BLANK

PAGE

Preface

The present report describes the technique of inelastic neutron scattering and the application of this technique to the study of the magnetic excitations in rare earth metals. This work represents some of the most recent measurements carried out at the Risø Triple-Axis-Spectrometer.

The design of this spectrometer was started in 1961 by L. Passell and the author. The construction was completed in 1964, and from that time the spectrometer has been used in inelastic neutron scattering measurements. A list of publications of the results of this work is given below.

The experiments described in this report were carried out in the period from the beginning of 1965 to the summer of 1967. Short reports on the main experimental results have already been published (III, IV and VI of the list below).

List of publications on inelastic neutron scattering measurements carried out the Risø Triple-Axis-Spectrometer

I. H. Bjerrum Møller and A. R. Mackintosh
Inelastic Scattering of Neutrons in Chromium.
Inelastic Scattering of Neutrons, Vol. 1, p. 95 (I. A. E. A., Vienna, 1965).

II. H. Bjerrum Møller and A. R. Mackintosh
Observation of Resonant Lattice Modes by Inelastic Neutron Scattering.
Phys. Rev. Letters 15, 623 (1965).

III. H. Bjerrum Møller and J. C. Gylden Houmann
Inelastic Scattering of Neutrons by Spin Waves in Terbium.
Phys. Rev. Letters 17, 737 (1966).

IV. H. Bjerrum Møller, J. C. Gylden Houmann and A. R. Mackintosh
Magnetic Interactions in Rare Earth Metals from Inelastic. Neutron Scattering.
Phys. Rev. Letters 19, 312 (1967).

V. A. R. Mackintosh and H. Bjerrum Møller
Investigations of Localized Excitations by Inelastic Neutron Scattering.
Proceedings of the International Conference on Localized Excitations in Solids.
University of California, Irvine (1967).

VI. H. Bjerrum Møller, J. C. Gylden Houmann and A. R. Mackintosh
Magnetic Interactions in Tb and Tb-10% Ho from Inelastic Neutron Scattering.
Proceedings of the International Congress on Magnetism, Journal of Applied Physics (1968).

I. Introduction

The ions of the heavy rare earth metals generally carry a large magnetic moment, because the 4f electronic shell is incompletely filled. These moments are highly localized, and there is therefore no appreciable direct exchange interaction between them in the metal. There is, however, a strong indirect interaction between them, established through the medium of the conduction electrons. The spatial form of this indirect exchange interaction is determined primarily by the properties of the conduction electron gas, and it produces unusual and complex magnetic structures below certain characteristic ordering temperatures.

The correlated thermal motion of the localized moments at finite temperatures can be described in terms of elementary magnetic excitations, which interact only weakly with each other. These excitations have the form of spin waves, in which a small sinusoidally varying deviation of the moment from the completely ordered state travels through the lattice. The spin wave quantum is called a magnon, in analogy with the phonon, which is a lattice wave quantum. The excitation of a single magnon reduces the ordered moment of the system by one Bohr magneton.

In the approximation in which the magnon interactions are neglected, the lifetimes of the magnons are infinite and they therefore have a well defined energy $\epsilon(\mathbf{q}) = \hbar\omega(\mathbf{q})$ and momentum $\hbar\mathbf{q}$, where $\mathbf{q}$ and $\omega(\mathbf{q})$ are respectively the wavevector and angular frequency. The relation $\epsilon(\mathbf{q})$ between ϵ and $\mathbf{q}$ is called the dispersion relation and is determined primarily by the exchange forces. Since thermal neutrons may excite or absorb a magnon in a scattering process in which momentum and energy are conserved, the magnon dispersion relation may be determined from a study of the change in momentum and energy of the neutrons in the scattering process. In this way, neutron scattering may be used to obtain information on the exchange forces.

The interactions of magnons with each other and with phonons, electrons or impurities in the lattice may limit the magnon lifetime, and hence give rise to a natural energy width in the neutron groups observed in inelastic neutron scattering. A study of this linewidth therefore provides information on the

magnon interactions. These interactions may also perturb the magnon dispersion relation and the nature of the perturbation provides further information on the form of the interaction.

The present paper describes an experimental investigation of these magnetic interactions in Tb and an alloy of Tb with 10% Ho, by the technique of inelastic neutron scattering. As an introduction, we review briefly the relevant parts of the theory of the magnetism of the rare earth metals and discuss the various types of neutron scattering processes which may occur. The cross section for each of these processes is given. Chapter II describes the experimental method, with especial attention to those features of the technique which allow an accurate determination of the energies and lifetimes of the magnons. The interpretation of these data is discussed in chapter III, with special reference to the relation between the conduction electron band structure and the indirect exchange interaction between the magnetic ions. The interaction between the magnons and electrons, phonons and impurities is also considered.

1. Magnetism of Rare Earth Metals

Neutron diffraction measurements by Koehler et al.[1-3] have shown that the rare earth metals have interesting and unusual magnetic structures. Terbium, for instance, has temperature regions of paramagnetic, antiferromagnetic and ferromagnetic ordering. The configuration of the moments in the ordered phases is shown in Fig. 1.

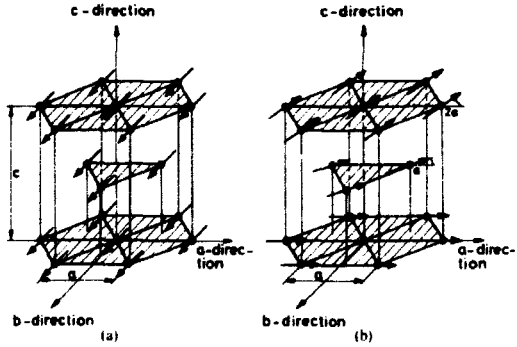

Fig. 1. The magnetic structure in terbium
(a) in the ferromagnetic phase $T < T_C$
(b) in the spiral phase (turn angle φ) $T_C < T < T_N$

The crystal structure is hexagonal closed packed with a = 3.599 Å and c = 5.696 Å at 300°K. Below the Curie temperature T_C the magnetic structure is ferromagnetic with all moments aligned along the b-direction (see Fig. 1a). In the temperature region from T_C to the Néel temperature T_N, the magnetic moments form a spiral structure (see Fig. 1b), in which the moments remain aligned in the plane containing the a- and b-direction (called the basal plane), but change direction from one layer of atoms to the next by an angle λ, called the interplanar turn angle. The spiral structure can be characterized by its wavevector **Q**, defined as a vector in the c-direction of magnitude $\frac{4\pi}{c}\frac{\lambda}{360}$ (λ is measured in degrees). Above the Néel temperature the magnetic structure is paramagnetic.

The localized magnetic moments of the rare earth metals are due to the electrons of the unfilled 4f shell. The radius of the 4f shell is small compared to the interatomic distances, so overlap between neighboring 4f shells is very small. The interaction between the localized moments is therefore believed to be mainly an indirect exchange interaction via the conduction electrons. Each localized moment produces a spin polarization of the conduction electrons which in turn interacts with another moment.

The theory of indirect exchange was first studied by Ruderman and Kittel[3], Kasuya[4] and Yosida[5]. They showed that the exchange Hamiltonian can be written in the form

$$H_{ex} = -\sum_{l>m} J(\mathbf{R}_l - \mathbf{R}_m)\ \mathbf{J}_l \cdot \mathbf{J}_m \tag{1}$$

where $\mathbf{J}_l$ is the total angular momentum operator for the l'th atom and the indirect exchange parameter $J(\mathbf{R}_l - \mathbf{R}_m)$ is a long range oscillatory function of the separation between the atoms.

For a general conduction electron band structure the Fourier transform of the indirect exchange parameter

$$J(\mathbf{q}) = \sum_{l} J(\mathbf{R}_l)\, e^{i\mathbf{q}\cdot\mathbf{R}_l} \tag{2}$$

is given by an expression of the form[6]

$$J(\mathbf{q}) = \sum_{n,n';\mathbf{k}} \frac{I_{nn'}(\mathbf{k},\mathbf{k}+\mathbf{q}+\boldsymbol{\tau})\ f(\varepsilon_n(\mathbf{k}))\ [1-f(\varepsilon_{n'}(\mathbf{k}+\mathbf{q}+\boldsymbol{\tau}))]}{\varepsilon_{n'}(\mathbf{k}+\mathbf{q}+\boldsymbol{\tau})-\varepsilon_n(\mathbf{k})} \tag{3}$$

where $\epsilon_n(\mathbf{k})$ is the energy of a Bloch state of wavevector $\mathbf{k}$ in band n, $I_{nn'}(\mathbf{k}, \mathbf{k}-\mathbf{q}+\tau)$ is a slowly varying function and τ is a reciprocal lattice vector chosen so that $\mathbf{q}$ lies in the first Brillouin zone. $f(\epsilon)$ is the Fermi function

$$f(\epsilon) = \frac{1}{e^{(\epsilon-\epsilon_F)/kT}+1} \tag{4}$$

where ϵ_F is the Fermi energy and T the temperature.

Kaplan[7] took anisotropy of the exchange interaction into account by adding the term

$$-\sum_{l,m} K_{lm} J_{zl} J_{zm} \tag{5}$$

to the exchange Hamiltonian (1), where J_{zl} is the c-component of $\mathbf{J}_l$. The resulting Hamiltonian is then the most general quadratic function of the angular moments of two atoms in a structure with hexagonal symmetry.

The anisotropy of the exchange interaction arises because of the orbital angular momentum, which is not quenched in most of the heavy rare earth metals. However, Kaplan and Lyons[8] showed that the anisotropy of the exchange is probably small.

The fact that the rare earth metals have an orbital angular moment, and therefore a nonspherical distribution of the 4f electrons, also gives rise to an anisotropic crystalline field, which is very important in determining their magnetic structures.

The crystalline field anisotropy energy is discussed by Elliott[9] and Miwa and Yosida[10]. Its contribution to the Hamiltonian can be written phenomenologically as

$$H_a = \sum_l \left\{ B J_{zl}^2 + D J_{zl}^4 + F J_{zl}^6 - \tfrac{1}{2} G \left[(J_{xl}+iJ_{yl})^6 + (J_{xl}-iJ_{yl})^6 \right] \right\} \tag{6}$$

which is the most general function of the moment of a single atom of order six and with hexagonal symmetry. That part of the exchange anisotropy for which $l = m$ in (5) is included in the crystal field anisotropy term. We will neglect the second and the third term ($D = F = 0$). With positive B and G the crystal field anisotropy energy will be minimized when the moments lie in the basal hexagonal plane and point in the x-direction.

Yoshimori[11], Villain[12] and Kaplan[13] then explained the magnetic structures

of Tb (and the other heavy rare earth metals) and the transitions between different magnetic structures on the basis of the Hamiltonian

$$H = H_{ex} + H_a \tag{7}$$

in terms of the "competition" of the positive interaction between the nearest atomic neighbors, and of the negative interaction between the next nearest neighbors from the long range oscillatory indirect exchange interaction. Yosida and Miwa[14] expressed this in terms of the Fourier transformed exchange parameter $J(\mathbf{q})$, and showed that, if the six fold anisotropy is neglected ($G = 0$), the spiral structure will be stable with wavevector $\mathbf{Q}$, if $J(\mathbf{q})$ has an absolute maximum for $\mathbf{q} = \mathbf{Q}$. The six fold anisotropy will of course tend to prevent the formation of a spiral structure by keeping the spin in the x-direction (if G is positive).

Most of the theories[15] assume therefore that the transition from spiral structure to ferromagnetic structure takes place when the six fold anisotropy, which is strongly temperature dependent, reaches a certain strength.

As may be seen from the expression (3), the maximum in $J(\mathbf{q})$ and hence the $\mathbf{Q}$ of the spiral phase is determined by the band structure. Of especial importance are terms with a small energy denominator, and these arise when $\mathbf{q}$ spans some dimension of the Fermi surface. From a consideration of the band structures of the heavy rare earth metals, Williams, Loucks and Mackintosh[16] suggested that the maximum in $J(\mathbf{q})$ is determined by the separation in $\mathbf{k}$ space of flat regions of the Fermi surface.

Niira[17], Yosida and Miwa[14] and others[18,19] carried out an approximate diagonalization of the Hamiltonian and found expressions for the magnon dispersion relations. For the c-direction the expressions are

$$\nu(\mathbf{q}) = J\left[(J(0)-J(\mathbf{q}))^2 + 2(B + 21GJ^4)(J(0)-J(\mathbf{q})) + 72\,GJ^4(B + 3GJ^4)\right]^{1/2} \tag{8}$$

$$\nu(\mathbf{q}) = J\left\{\left[J(\mathbf{Q}) - {}^1\!/_2 J(\mathbf{Q}+\mathbf{q}) - {}^1\!/_2 J(\mathbf{Q}-\mathbf{q})\right]\left[J(\mathbf{Q})-J(\mathbf{q}) + 2B\right]\right\}^{1/2} \tag{9}$$

for the ferromagnetic and spiral phases respectively. We have here used the double zone representation in which $\mathbf{q}$ runs from zero to twice the distance to the primitive zone boundary in the c-direction, so that the magnon dispersion relation consists of one continuous branch in this direction.

It is seen from these expressions that measurements of the magnon dispersion

relations give detailed information on the indirect exchange interactions. The primary object of the present paper is to describe such measurements and correlate the results with the theory.

2. *Neutron Scattering*

Thermal neutrons impinging on a crystal may undergo various types of scattering processes. In a magnetic crystal the scattering may be caused by a nuclear interaction or by a magnetic interaction. The scattering process may occur with no change of energy between the incident and scattered neutrons, or the neutrons may exchange energy with the crystal. These two types of scattering are referred to as elastic and inelastic neutron scattering, respectively. Both nuclear and magnetic scattering may be elastic or inelastic. In inelastic scattering through the nuclear interaction the neutrons create or destroy phonons, whereas either phonons or magnons may be excited through the magnetic interaction.

Because of the periodic structure of the lattice, it is possible for the scattered neutrons to interfere with each other coherently, and produce peaks in the scattered neutron intensity for certain momentum and energy transfers. Deviations from ideal periodicity, such as differences of the neutron scattering from equivalent crystallographic sites because of nuclear spin, atomic, magnetic or isotopic disorder, will act to destroy the coherent nature of the scattering and contribute an incoherent background to the coherently scattered neutrons.

The general theory of neutron scattering by crystals was first treated by Weinstock[20] and by Halpern and Johnson[21]. The neutron scattering cross sections were calculated in the Born approximation, using a Fermi pseudopotential[22]

$$V(\mathbf{r}) = \frac{2\pi\hbar^2}{m} a_S \, \delta(\mathbf{r}) \tag{10}$$

to describe the nuclear interaction between the neutron and the nuclei, whereas the magnetic interaction was calculated as the interaction of the magnetic field produced by the neutron with the electron current due to the unclosed shells of the scattering atoms. A list of symbols is given on page 17.

The elastic scattering cross section of an atom per unit solid angle, for unpolarized neutrons was shown to be

$$\frac{d\sigma}{d\Omega} = a_S^2 + (1 - e_n^2)\, a_M^2(\varkappa) \tag{11}$$

where the magnetic scattering amplitude is

$$a_M(\varkappa) = \tfrac{1}{2} r_0 \gamma g J f(\varkappa) \tag{12}$$

The nuclear scattering amplitude a_N is independent of $\varkappa$, while the magnetic scattering amplitude $a_M(\varkappa)$ depends on $\varkappa$ through the magnetic formfactor $f(\varkappa)$. Since this is essentially the Fourier transform of the unpaired electron distribution, it decreases with increasing $\varkappa$.

The neutron cross sections for the various neutron scattering processes have later been derived in a number of papers. Below are given the coherent cross sections, relevant to this work:

Elastic Nuclear Scattering[23]

$$\frac{d\sigma}{d\Omega} = a_N^2 \frac{(2\pi)^3}{2V} e^{-2W} \sum_{\tau} |F(\tau)|^2 \delta(\varkappa - \tau) \tag{13}$$

Elastic Magnetic Scattering from Ferromagnetic Structure[23]

$$\frac{d\sigma}{d\Omega} = a_M^2(\varkappa) \frac{(2\pi)^3}{2V} e^{-2W} (1 - e_m^2) \left(\frac{J(T)}{J} \right)^2 \sum_{\tau} |F(\tau)|^2 \delta(\varkappa - \tau) \tag{14}$$

Elastic Magnetic Scattering from Spiral Structure[23]

$$\frac{d\sigma}{d\Omega} = \frac{1}{4} a_M^2(\varkappa) \frac{(2\pi)^3}{2V} e^{-2W} (1 \mp e_Q^2) \left(\frac{J(T)}{J} \right)^2 \sum_{\tau} |F(\tau)|^2 [\delta(\varkappa \cdot Q - \tau) + \delta(\varkappa - Q - \tau)] \tag{15}$$

One-Phonon Creation (through Nuclear Interaction)[23]

$$\frac{d^2\sigma}{d\Omega dE} = \frac{k_2}{k_1} a_N^2 \frac{(2\pi)^3}{N_a V} e^{-2W} \frac{\hbar^2 \varkappa^2 (e \cdot \ell_{q,i})^2}{2M\varepsilon_i(q)} \left[n_i(q) + 1 \right] |F_i(\varkappa)|^2 \sum_{\tau} \delta(\varkappa - q - \tau) \delta(E - \varepsilon_i(q)) \tag{16}$$

One-Phonon Creation (through Magnetic Interaction)[24] from Ferromagnetic Structure (Magnetovibrational Scattering)

$$\frac{d^2\sigma}{d\Omega dE} = \frac{k_2}{k_1} a_M^2(\varkappa) \frac{(2\pi)^3}{N_a V} e^{-2W} (1 - e_m^2) \left(\frac{J(T)}{J}\right)^2 \frac{\hbar^2 \varkappa^2 (e \cdot \xi_{q,s})^2}{2M\varepsilon_s(q)}$$
$$[n_s(q) + 1] |F_s(\varkappa)|^2 \sum_\tau \delta(\varkappa - q - \tau)\, \delta(E - \varepsilon_s(q)) \qquad (17)$$

One-Phonon Creation (through Magnetic Interaction) from Spiral Structure

$$\frac{d^2\sigma}{d\Omega dE} = \frac{k_2}{k_1} a_M^2(\varkappa) \frac{(2\pi)^3}{N_a V} e^{-2W} (1 - e_Q^2) \left(\frac{J(T)}{J}\right)^2 \frac{\hbar^2 \varkappa^2 (e \cdot \xi_{q,s})^2}{2M\varepsilon_s(q)}$$
$$[n_s(q) + 1] |F_s(\varkappa)|^2 \sum_\tau \tfrac{1}{2} [\delta(\varkappa - q + Q - \tau) + \delta(\varkappa - q - Q - \tau)]$$
$$\delta(E - \varepsilon_s(q)) \qquad (18)$$

One-Magnon Creation from Ferromagnetic Structure[23]

$$\frac{d^2\sigma}{d\Omega dE} = \frac{k_2}{k_1} a_M^2(\varkappa) \frac{(2\pi)^3}{N_a V} e^{-2W} \frac{1}{2J} [n_s(q) + 1] (1 + e_m^2)$$
$$|F_s(\varkappa)|^2 \sum_\tau \delta(\varkappa - q - \tau)\, \delta(E - \varepsilon_s(q)) \qquad (19)$$

One-Magnon Creation from Spiral Structure[25]

$$\frac{d^2\sigma}{d\Omega dE} = \frac{k_2}{k_1} a_M^2(\varkappa) \frac{(2\pi)^3}{N_a V} e^{-2W} \frac{1}{2J} [n_s(q) + 1] |F_s(\varkappa)|^2$$
$$\sum_\tau \left\{ \frac{1}{4} (1 + e_Q^2)\, A(q) [\delta(\varkappa - q - Q - \tau) + \delta(\varkappa - q + Q - \tau)] \right.$$
$$\left. + (1 - e_Q^2)\, B(q)\, \delta(\varkappa - q - \tau) \right\} \delta(E - \varepsilon_s(q)) \qquad (20)$$

where

$$A(q) \quad \frac{1}{B(q)} \quad \sqrt{\frac{J(Q) - J(q)}{J(Q) - \tfrac{1}{2} J(Q + q) - \tfrac{1}{2} J(Q - q)}} \qquad (21)$$

for excitation of magnons in the c-direction[25].

The following symbols have been used in equations (10)-(21):

a_M	magnetic scattering amplitude
a_N	nuclear scattering amplitude
$\mathbf{e}$	unit vector in direction of $\varkappa$
e_m	component of $\mathbf{e}$ in the magnetization direction
e_Q	component of $\mathbf{e}$ along $\mathbf{Q}$
e^{-W}	Debye-Waller factor
E	neutron energy transfer, $E = \frac{\hbar^2}{2m}(k_1^2 - k_2^2)$
$f(\varkappa)$	magnetic formfactor
$F(\tau)$	geometrical structure factor for elastic scattering
$F_\lambda(\varkappa)$	geometrical structure factor for inelastic scattering
g	Landé factor, $g = \frac{3}{2} - \frac{S(S+1) - L(L+1)}{2J(J+1)}$
J	total angular momentum of the atoms
J(T)/J	relative ordered moment as a function of T
$\mathbf{k}_1$	wavevector of incident neutrons
$\mathbf{k}_2$	wavevector of scattered neutrons
L	orbital angular momentum of the atoms
m	mass of the neutron
M	mass of the atoms
$n_\lambda(\mathbf{q})$	number of thermally excited magnons or phonons
N_a	number of atoms in the crystal
$\mathbf{q}$	magnon or phonon wavevector
$\mathbf{Q}$	wavevector of the spiral structure
r_0	electromagnetic radius of the electron, $r_0 = 2.82 \cdot 10^{-13}$ cm
S	spin angular momentum of the atoms
T	temperature of the crystal
V	volume of the unit cell
γ	magnetic moment of neutron in nuclear magnetons, $\gamma = -1.913$
$\varepsilon_\lambda(\mathbf{q})$	magnon or phonon energy
$\varkappa$	neutron scattering vector, $\varkappa = \mathbf{k}_1 - \mathbf{k}_2$
λ	branch of magnon or phonon dispersion relation
Ω	solid angle of scattering
$\boldsymbol{\ell}_{\mathbf{q}\lambda}$	unit polarization vector of phonons
σ	neutron scattering cross section
τ	reciprocal lattice vector

The cross sections are given per atom and per unit solid angle of scattering. The inelastic cross sections are further per unit energy transfer of the scattered neutrons. We have assumed pure Heisenberg exchange between the magnetic ions and neglected magnon and phonon interactions. Only the creation cross sections have been given, since all measurements were performed with neutron energy loss, and only one-phonon and one-magnon cross sections are considered, since multiple phonon and magnon processes only contribute a smoothly varying background to the neutron peaks observed from the above processes.

The cross sections are expressed in the reciprocal lattice, which is derived from the real lattice through the relation

$$\tau \cdot \mathbf{a}_i = 2\pi p \tag{22}$$

where p is an integer, $\mathbf{a}_i$ is any of the basis vectors $\mathbf{a}_1$, $\mathbf{a}_2$, $\mathbf{a}_3$ of the crystal lattice

$$\tau = h\mathbf{b}_1 + k\mathbf{b}_2 + l\mathbf{b}_3 \tag{23}$$

where h, k and l are integers (Miller indices) and τ is a vector of the reciprocal lattice with basis vectors $\mathbf{b}_1$, $\mathbf{b}_2$ and $\mathbf{b}_3$.

It follows from (22) that

$$\mathbf{b}_1 = 2\pi \frac{\mathbf{a}_2 \cdot \mathbf{a}_3}{\mathbf{a}_1 \cdot \mathbf{a}_2 \cdot \mathbf{a}_3} \qquad \mathbf{b}_2 = 2\pi \frac{\mathbf{a}_3 \cdot \mathbf{a}_1}{\mathbf{a}_1 \cdot \mathbf{a}_2 \cdot \mathbf{a}_3} \qquad \mathbf{b}_3 = 2\pi \frac{\mathbf{a}_1 \cdot \mathbf{a}_2}{\mathbf{a}_1 \cdot \mathbf{a}_2 \cdot \mathbf{a}_3} \tag{24}$$

The δ-functions in reciprocal space give the directions in which neutrons scatter coherently.

When the basic unit cell contains two atoms, there will exist two branches of the dispersion relation, called acoustic and optical respectively. In an optical phonon mode of small wavevector $\mathbf{q}$, the two atoms of the unit cell vibrate against each other, but the centre of mass of the cell is fixed. If the two ions are oppositely charged a motion of this kind may be excited by the electric field of a light wave. In the acoustic phonon mode of small $\mathbf{q}$, the two atoms of the unit cell move together, as in a sound wave vibration. The energy of the acoustic mode is zero for $\mathbf{q} = 0$, with a slope determined from the velocity of sound. Optical and acoustic magnon modes are defined in analogy with the phonon modes, with the lattice displacement replaced by the precession of the magnetic moment.

The dispersion relations for acoustic and optical phonons each consist of three branches determined by the polarization of the modes (direction of

vibration relative to q). For directions of high symmetry, these are one longitudinal and two transverse branches. For magnons there is no equivalent of the polarization of phonons. The symbol λ is used to label the branch of the dispersion relation.

Both magnons and phonons are bosons, so that the number n(q) of thermally excited magnons or phonons of wavevector q in the branch λ, at temperature T is

$$n_\lambda(\mathbf{q}) = \left[\exp\frac{\epsilon_\lambda(\mathbf{q})}{kT} - 1\right]^{-1} \tag{25}$$

In a crystal containing two atoms per basic unit cell, the neutrons scattered from the two sublattices may interfere constructively or destructively. This is expressed by the geometrical structure factor which, for elastic scattering, takes the form

$$|F(\tau)|^2 = 2\,(1 + \cos \tau \cdot \varrho) \tag{26}$$

where ϱ is the vector between the two atoms in the unit cell.

The geometrical structure factor for inelastic neutron scattering is defined everywhere in reciprocal space and depends on the branch of the excitation. For magnon scattering from a ferromagnetic hexagonal closed packed lattice it can be shown to be[26]

$$\begin{aligned} |F_a(\varkappa)|^2 &= 2\cos^2{}^1/_2\left\{-\tau\cdot\varrho + \Phi(\mathbf{q})\right\} \\ |F_o(\varkappa)|^2 &= 2\sin^2{}^1/_2\left\{-\tau\cdot\varrho + \Phi(\mathbf{q})\right\} \end{aligned} \tag{27}$$

for the acoustic and optical branch, respectively.

Here

$$\cos\Phi(\mathbf{q}) = \frac{1}{2}\left|\sqrt{\frac{J'^*(\mathbf{q})}{J'(\mathbf{q})}} + \sqrt{\frac{J'(\mathbf{q})}{J'^*(\mathbf{q})}}\right| \tag{28}$$

where

$$J'(\mathbf{q}) = \sum_{\mathbf{R}_{1'}} J(\mathbf{R}_{1'})\, e^{i\mathbf{q}\cdot\mathbf{R}_{1'}}$$

and the sum extends over all vectors from one atom to all the atoms in the other sublattice.

II. Experimental Technique

The expressions for the neutron cross sections show that a necessary condition for elastic coherent neutron scattering ($|\mathbf{k}_1| = |\mathbf{k}_2|$) is that

$$\mathbf{\kappa} = \boldsymbol{\tau} \tag{29}$$

This condition is illustrated by the vector diagram shown in Fig. 2.

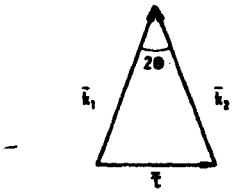

Fig. 2. Vector diagram for Bragg scattering.

which gives the Bragg relation[27]

$$|\boldsymbol{\tau}| = 2|\mathbf{k}_1| \sin\theta$$

or

$$n\frac{2\pi}{k_1} = n\lambda = 2d\sin\theta \tag{30}$$

for coherent elastic reflection from lattice planes spaced by the distance

$$d = \frac{2\pi}{\tau}$$

n is an integer, which enters the expression because $n\boldsymbol{\tau}$ is also a reciprocal lattice vector.

Bragg reflection of monochromatic neutrons therefore gives peaks in the scattered neutron intensity at scattering angles determined from (30).

The conditions for inelastic coherent neutron scattering are

$$\mathbf{q} = \mathbf{\kappa} - \boldsymbol{\tau} \tag{32}$$

and

$$\epsilon(\mathbf{q}) = \frac{\hbar^2}{2m}(k_1^2 - k_2^2) = E \tag{33}$$

The first of these conditions (momentum conservation) is illustrated by the following vector diagram in reciprocal space.

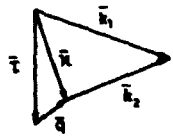

Fig. 3. Vector diagram for the excitation of a magnon (or phonon) of wavevector $\mathbf{q}$.

If the second condition (energy conservation) is fulfilled at the same time, a coherent neutron scattering process will take place, and a peak in the scattered neutron intensity will be observed.

The natural variables of a neutron scattering experiment are therefore seen to be the wavevector $\mathbf{q}$ and the energy transfer E, and a measurement of the dispersion relation $\epsilon(\mathbf{q})$ consists of finding peaks in the scattered neutron intensity in $\mathbf{q}$-E-space. Such a series of measurements, in which $\mathbf{q}$ and/or E are varied, and the scattered neutron intensity measured, will be refered to as a scan in $\mathbf{q}$-E-space.

In order to perform such scans, it is necessary to have control over the length and direction of the incident and scattered neutron wavevectors and the orientation of the sample.

The necessary energy selection can be achieved by Bragg reflection from a single crystal (using (30)). This principle is utilized in the triple-axis-spectrometer shown schematically in Fig. 4. This type of apparatus was first developed by Brockhouse[28] and used primarily in phonon dispersion relation measurements.

However, if E_0 is small compared to the energy of the scattered neutrons and $|\mathbf{q}_0|$ is small compared to $|\mathbf{k}_2|$, these corrections can be neglected, and the resolution function measured on a Bragg reflection can be assumed applicable to the inelastic scattering measurements. This was the case for most of the measurements described in this report.

3. Focusing

The width of the neutron groups observed in different scans may differ widely, due to the correlation between $\mathbf{q}$ and E in the experimental resolution function. This phenomenon is known as focusing, and analytical and graphical methods have been developed to predict the spectrometer conditions that will give optimum focusing[31, 32].

This information and the instrumental width for any scan are however immediately obtained from knowledge of the resolution ellipsoid defined in the preceeding section. This is illustrated in Fig. 14.

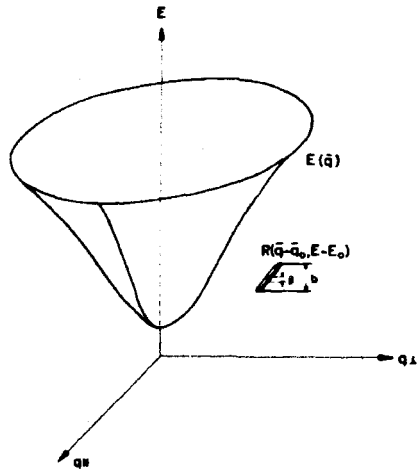

Fig. 14. Dispersion surface and resolution ellipsoid for $\mathbf{q}$-vectors in the scattering plane. In constant $\mathbf{q}$-scans the resolution ellipsoid is moved vertically through the dispersion surface.

The surface shown is the dispersion relation $E(\mathbf{q})$ for $\mathbf{q}$ lying in the scattering plane. The resolution ellipsoid is also shown. In a constant $\mathbf{q}$ scan the ellipsoid is moved vertically, and a peak is observed when it crosses the $E(\mathbf{q})$ surface. Assuming infinite lifetime of the excitations, the width of this peak depends on the range of E over which the crossing occurs. The width is seen to be minimum if the constant $\mathbf{q}$-scan is measured with $\mathbf{q}$ perpendicular to $\varkappa$ (on the positive $q_{\perp}$ axis), the width being β if the slope of the dispersion surface at the crossing point is parallel to the major axis of the resolution ellipsoid. The maximum width is seen when $\mathbf{q}$ is along the negative $q_{\perp}$ axis, and the width b is observed for $\mathbf{q}$ parallel to $\varkappa$. These three cases are referred to as focusing, defocusing and non-focusing scans respectively. Various degrees of focusing and defocusing exist. The same effects occur in constant E-scans, where the resolution ellipsoid is moved parallel to the scattering plane.

We conclude therefore that knowledge of the resolution function and the slope of the dispersion relation allows one to predict the resolution width for any scan. This is important when choosing the most favorable scan and, in addition, it allows a determination of the natural width of the neutron groups.

4. Intensities

In order to find the observed inelastic neutron scattering cross sections σ_{in} we must average the cross section over the resolution function.

With the spectrometer set at $\mathbf{q}_0$, E_0 we find

$$\sigma_{in} = \Omega B \int\int \sum_{\mathbf{q}_{j\varkappa}} \delta(\mathbf{q}-\mathbf{q}_{j\varkappa})\, \delta(E-\epsilon(\mathbf{q}_{j\varkappa}))\, R(\mathbf{q}-\mathbf{q}_0, E-E_0)\, d\mathbf{q}dE \quad (36)$$

where the slowly varying proportionality constant B is the factor multiplying the δ-functions in (16), (17) and (19) for phonon, magnetovibrational and magnon scattering, respectively. $\mathbf{q}_{j\varkappa}$ is the wavevector of the excitation (phonon or magnon) and $\epsilon(\mathbf{q}_{j\varkappa})$ its energy. Ω is the solid angle of scattering ($\approx 5 \cdot 10^{-4}$ steradians).

The summation over $\mathbf{q}_{j\varkappa}$ is transformed to an integration by multiplying by the density of end points of $\mathbf{q}_{j\varkappa}$-vectors in reciprocal space

$$\sigma_{in} = \Omega B \frac{NV}{(2\pi)^3} \int R(\mathbf{q}_{j\varkappa}-\mathbf{q}_0, \epsilon(\mathbf{q}_{j\varkappa}) - E_0)\, d\mathbf{q}_{j\varkappa} \quad (37)$$

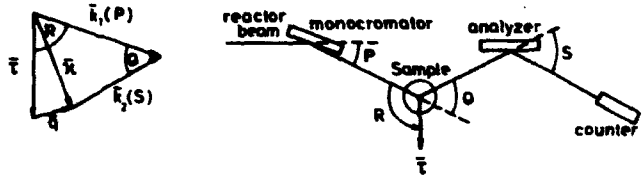

Fig. 4. Schematic diagram of the triple-axis-spectrometer.

The monochromatic incident neutron beam is extracted from the reactor spectrum by Bragg reflection from a single crystal, the monochromator crystal. The energy of the monochromatic neutrons (and therefore the length of the $\mathbf{k}_1$-vector) is determined by the angle P. The neutrons scatter from the sample through the angle Q, and the energy of the scattered neutrons (or the length of $\mathbf{k}_2$) is determined by the angle S. Finally the angle R determines the orientation of the sample crystal relative to the incident neutron direction.

It is possible with the triple-axis-spectrometer to perform scans in which one of the natural variables is varied while the other is fixed.

Two such scans are represented in Figs. 5 and 6, where three of the configurations of the spectrometer are shown for each scan. Fig. 6 shows a constant $\mathbf{q}$-scan in which the $\mathbf{q}$-vector is fixed and the energy transfer varied. Fig. 5 shows a constant E-scan in which the energy and direction of $\mathbf{q}$ are fixed and the magnitude of $\mathbf{q}$ varied. The intensity of the scattered neutrons, as a function of energy transfer and wavevector respectively, shows peaks when (32) and (33) are simultaneously satisfied. These peaks are superposed on a generally

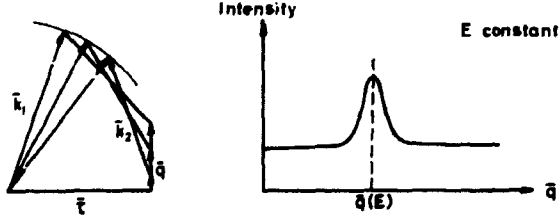

Fig. 5. Diagram illustrating a constant E scan.

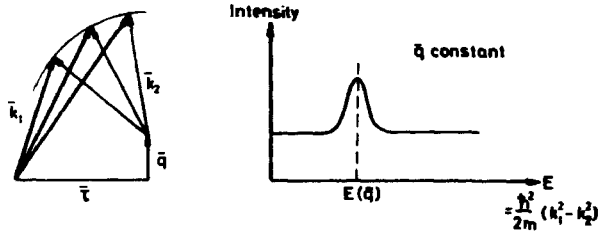

Fig. 6. Diagram illustrating a constant q scan.

smoothly varying background due to incoherent scattering, multiple phonon and magnon scattering and other processes.

It is also possible to perform an inelastic neutron scattering experiment on a spectrometer, where the energy selection is done by use of a neutron chopper and time-of-flight analysis. However, with such a spectrometer it is not possible to perform scans in which the direction of q is fixed. It is therefore less suited for investigations of solids in the form of single crystals, where it is important to be able to restrict measurements to symmetry directions, because this simplifies the analysis of the results.

This chapter describes the experimental details of the measurements of magnons in rare earth metals. The Risø triple-axis-spectrometer used for these measurements is first described. It is then shown that the experimental resolution function can be measured and that the instrumental width for any scan can be determined from this resolution function. The instrumental width is shown to depend very much on the scan so that "focusing" (i. e. narrow width) may occur for certain types of scan. The cross sections for production of inelastic and elastic neutron groups are calculated from the differential cross sections and the resolution of the spectrometer. The choice of scan is discussed and some of the most important sources of disturbing peaks are mentioned.

1. Description of the Triple-Axis-Spectrometer

The triple-axis-spectrometer shown in Figs. 7 and 8 was designed and constructed at Risø. It is installed at one of the horizontal tangential beam holes of the DR 3 reactor. The polychromatic neutron beam, incident upon the monochromator crystal, is obtained from a water scatterer placed in the

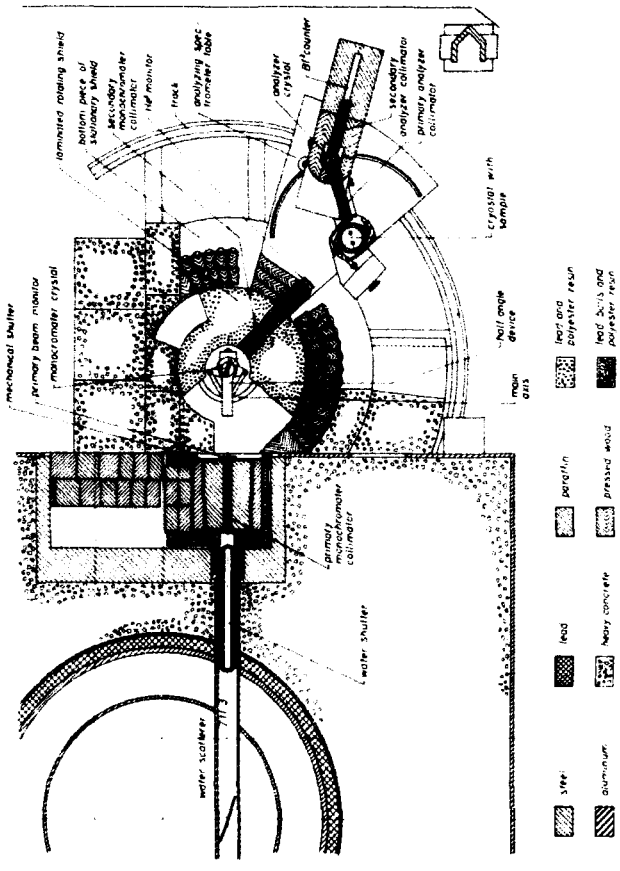

Fig. 7. The Risø triple-axis-spectrometer (horizontal view).

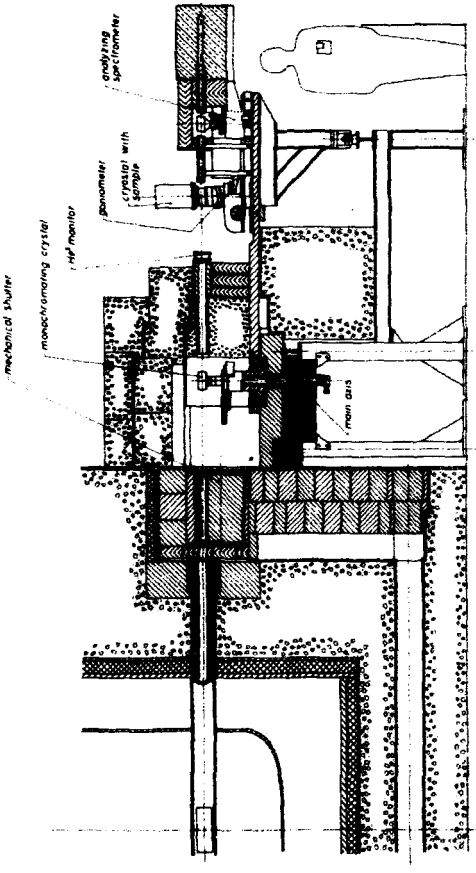

Fig. 8. The Risø triple-axis-spectrometer (vertical view).

beam tube at the position of maximum thermal neutron flux, approximately $6 \cdot 10^{13}$ n cm^{2}sec. The neutron scattering cross section of hydrogen for thermal neutrons is about 80 barns, while that for fast neutrons is about 20 barns. It is therefore possible to obtain a partial discrimination against fast neutrons in the neutron beam which is reflected to the spectrometer, by proper choice of the thickness of the water scatterer. This is important because shielding against fast neutrons is difficult. As the best compromise between high thermal neutron intensity and low fast neutron intensity, the thickness of the water scatterer was chosen such that it reflects about 90% of the thermal neutrons and about 10% of the fast neutrons.

A set of multichannel neutron collimators (Soller collimators) defines the directions of the neutron beam. The collimation of these collimators can be changed without loss of alignment by removing or adding plates.

Both the monochromator and analyzer are large single crystals of zinc (~ 20 cm $\cdot$ 8 cm $\cdot$ 2 cm) with the (002) planes parallel to the large face. They are mounted with the (002) planes in reflection and a mechanical coupling (half angle device) ensures that they remain in the reflecting position, when the scattering angle is varied.

All the four variable angles of the spectrometer (P, Q, R and S from Fig. 4) are set in position by electric motors and the positions are read to an accuracy of 1 minute of arc by means of shaft digitizers. The reproducibility in setting of the spectrometer is better than 1 minute of arc.

As seen from Figs. 7 and 8 the spectrometer is shielded heavily in order to bring down the background originating from neutrons which do not scatter through all the collimators. The heavy shielding is composed of hydrogeneous material (paraffin, pressed wood, polyester resin and concrete) and of lead (as shown in the figures) in order to shield against fast neutrons and gamma-rays, respectively. The thermal neutron background is easily shielded by thin sheets of cadmium (1 mm) or boron plastic (5 mm) which cover the heavy shielding around the monochromator and analyzer. The count rate of background neutrons, which penetrate this heavy shielding, is about 1 count per min.

Another contribution to the background, which cannot be shielded against, comes from neutrons which scatter through all collimators with an incoherent scattering process or a multiphonon or multimagnon scattering process in at least one of the three crystals (monochromator, sample or analyzer), or which scatter from other material than these three crystals, such as constructional material in the beam (for instance the cryostat). With the terbium sample in place, this part of the background is also about 1 count per min.

For the low temperature measurements the sample was placed in a liquid

nitrogen cryostat, in thermal contact with a liquid nitrogen bath. Temperatures above liquid nitrogen temperature could be obtained by applying current to heating coils placed around the sample. By means of a thermocouple controlled feed-back system the temperature of the sample was maintained constant to approximately 0.1°K.

The spectrometer operation is automatized and governed by punched tapes. One tape, the program tape, contains the orders, such as the angle settings and the reading sequence for counters, angles and temperatures. Two types of scans are used, constant $\mathbf{q}$-scans and constant E-scans. The program tape is common for all scans of the same type. Another tape, the input data tape at a second reader, contains the sequence of angles at which the spectrometer should be set in the particular scan. These angles are computed and the data tape produced by the Risø GIER computer, from complete information on the desired $\mathbf{q}$-vectors in reciprocal space and the energy transfers. The results of the measurements are punched on tape, which can be written out, plotted or used in processing the results.

2. *Experimental Resolution*

Because of the finite collimations in the triple-axis-spectrometer, there is, for a fixed position of the spectrometer, a spread of the $\mathbf{k}_1$ and $\mathbf{k}_2$ vectors around their average values $\mathbf{k}_{10}$ and $\mathbf{k}_{20}$. Also the direction of the τ-vector is uncertain because any real crystal consists of small blocks (mosaic blocks) with slightly different orientation, so that there will be a spread (mosaic spread) of the τ-vectors around the average τ_0. This introduces a finite resolution into the spectrometer, which is of importance because it influences the width of the observed neutron groups.

Calculations of the resolution, based on knowledge of the mosaic spreads and the collimations, have been performed[29, 30, 31]. However, as we shall show here, the experimental resolution function can also be measured directly with better accuracy in many cases.

If the spectrometer is set to create excitations of wavevector $\mathbf{q}_0$ measured from the reciprocal lattice point τ_0, by scattering of incoming neutrons of wavevector $\mathbf{k}_{10}$ to wavevector $\mathbf{k}_{20}$, there will be a distribution of all these vectors around the average vectors. As a result there will be a finite probability that the vector $\mathbf{q}$ from the endpoint of a τ-vector to the endpoint of a neutron scattering vector $\varkappa$ will differ from its average value $\mathbf{q}_0$, and that the energy transfer E will differ from the average energy transfer E_0 (see Fig. 9).

This probability function is called the resolution function

$$R(\mathbf{q}-\mathbf{q}_0, E-E_0)$$

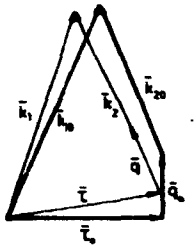

Fig. 9. Vector diagram showing how the finite collimations and mosaic spreads introduce an uncertainty in the $\mathbf{q}$-vector, because deviations of all vectors from their averages (labelled with subscript 0) are possible

It is a four-dimensional function of the natural variables $\mathbf{q}$ and E, and will in general also depend on $\mathbf{q}_0$ and E_0.

To find the observed intensity $I(\mathbf{q}_0, E_0)$ as a function of the settings of the spectrometer $\mathbf{q}_0$ and E_0, we have to fold the cross section for the scattering process $\sigma(\mathbf{q}, E)$ and the experimental resolution function $R(\mathbf{q}-\mathbf{q}_0, E-E_0)$

$$I(\mathbf{q}_0, E_0) = \int\int R(\mathbf{q}-\mathbf{q}_0, E-E_0)\, \sigma(\mathbf{q}, E)\, d\mathbf{q}dE \qquad (34)$$

In particular, if measurements are performed on a Bragg reflection, for which $\sigma(\mathbf{q},E) \propto \delta(\mathbf{q})\,\delta(E)$, we find the intensity

$$I^{Bragg}(\mathbf{q}_0, E_0) \propto R(-\mathbf{q}_0, -E_0) \qquad (35)$$

The resolution function $R(\mathbf{q}, E)$ can therefore be measured by mapping the Bragg reflected intensity as a function of the settings of the spectrometer, and this has been done for various collimations and settings of the Risø triple-axis-spectrometer.

A convenient way of representing the results of measurements of the four-dimensional resolution function is to plot contour lines for half peak intensity as a function of energy transfer E and wavevector $\mathbf{q}$, for fixed directions of $\mathbf{q}$. This has been done in Figs. 10 and 11 for three different directions of $\mathbf{q}$ and for two different resolutions of the spectrometer (different collimations and energy of incident neutrons).

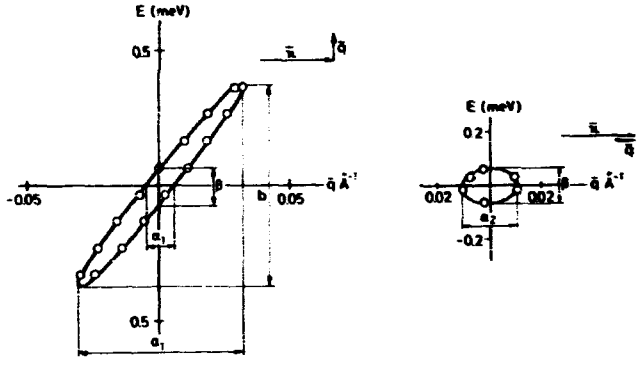

Fig. 10. Resolution ellipsoid measured at the [002] Bragg reflection with neutron energy 18.6 meV and the collimations 30', 40', 20', 25' counted from reactor to counter. The figure shows the resolution for the two directions of $\mathbf{q}$ in the scattering plane. For $\mathbf{q}$ perpendicular to the scattering plane the width of the resolution function is $\sigma_3 = 0.15$ Å^{-1} and no correlation exists between $\mathbf{q}$ and E.

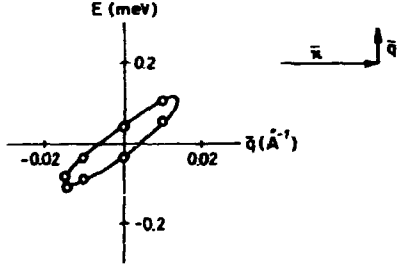

Fig. 11. Resolution ellipsoid measured at the [002] Bragg reflection with neutron energy 10 meV and the collimations 30', 25', 15', 15' counted from reactor to counter. The figure only shows the resolution for the direction of $\mathbf{q}$ for which correlation between $\mathbf{q}$ and E exists.

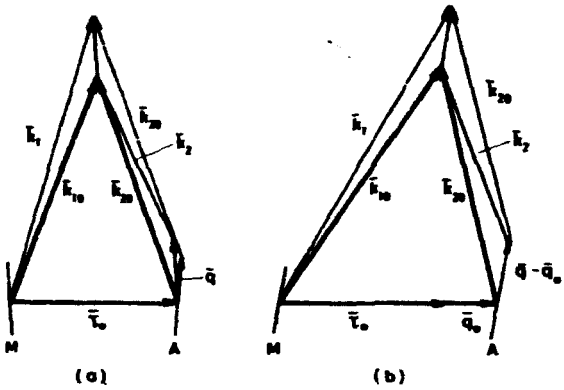

Fig. 12. Vector diagram illustrating the extension of the resolution function in the direction perpendicular to π, and the correlation between $\mathbf{q}$ and E for
(a) elastic scattering $\mathbf{q}_o = 0$, $E_o = 0$ (b) inelastic scattering $\mathbf{q}_o \neq 0$, $E_o \neq 0$.
Deviations of the incident neutron wavevector from $\mathbf{k}_{10}$ to $\mathbf{k}_1$ give rise to a $(\mathbf{q} - \mathbf{q}_o)$-vector approximately perpendicular to π and a larger energy transfer. Deviations of the scattered neutron wavevector from $\mathbf{k}_{20}$ to $\mathbf{k}_2$ have the same effect. M and A are the reflecting planes of the monochromator- and analyzer-crystal, respectively. $\mathbf{k}_1 - \mathbf{k}_{10}$ is parallel to M and $\mathbf{k}_2 - \mathbf{k}_{20}$ is parallel to A.

There is a very striking correlation between $\mathbf{q}$ and E for the component of $\mathbf{q}$ perpendicular to π, and this can be understood by consideration of Fig. 12(a).

The $\mathbf{k}_1$ vector in the figure has a smaller Bragg angle in the monochromator M than $\mathbf{k}_{10}$ and is therefore on average longer, giving a larger E. If $\mathbf{k}_{20}$ is now drawn from the endpoint of $\mathbf{k}_1$ it leads to a $\mathbf{q}$ vector different from the one the spectrometer is set at ($\mathbf{q}_o = 0$). If the incoming wavevector is $\mathbf{k}_{10}$ and the scattered wavevector $\mathbf{k}_2$ is taken to go through the collimator as shown in the figure, it will on average be shorter, giving the same E and approximately the same $\mathbf{q}$-vector. This $\mathbf{q}$-vector is therefore correlated with large E, as is observed.

Mosaic spreads in the monochromator and analyzer give a spread of the lengths of the $\mathbf{k}_1$- and $\mathbf{k}_2$-vectors for fixed directions, and are seen to give similar correlation effects.

Correlation between $\mathbf{q}$ and E can only occur for the component of the $\mathbf{q}$-vector in the scattering plane (defined by the $\mathbf{k}_{10}$ and $\mathbf{k}_{20}$-vectors), since the energies of the incoming and scattered neutrons are independent of the components of $\mathbf{k}_1$ and $\mathbf{k}_2$ perpendicular to the scattering plane.

We can therefore for many purposes neglect the component of $\mathbf{q}$ perpendicular to the scattering plane and visualize the half value contour surface of the resolution function as an ellipsoid in the remaining two components of $\mathbf{q}$ and the energy transfer. We will call this ellipsoid, shown in Fig. 13, the resolution ellipsoid.

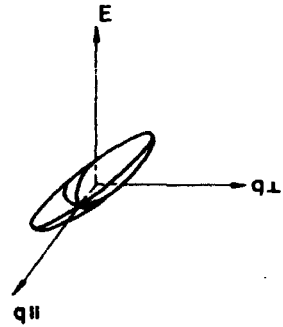

Fig. 13. The resolution ellipsoid.

We have now shown that the resolution function can be measured for $\mathbf{q}_0 = 0$ and $E_0 = 0$. Since the resolution function only depends on the distributions of $\mathbf{k}_1$ and $\mathbf{k}_2$ around their averages $\mathbf{k}_{10}$ and $\mathbf{k}_{20}$, it is a slowly varying function of $\mathbf{q}_0$ and E_0. Figure 12(b) illustrates the extension of the resolution function for an inelastic setting of the spectrometer, and it is seen that the resolution function is changed relative to the measured resolution function (Fig. 12(a)). The major axis of the resolution function is increased a little and is tilted slightly out of the $q_\perp E$ plane. Further, the angle between the major axis and the E-axis is decreased slightly.

Experimental information on some of these effects can be obtained from measurements of the resolution function at different reciprocal lattice points, and with different neutron energy, and corrections can be made if necessary.

The cross section for production of a single neutron group $\Delta E\sigma_{in}$ in a constant $\mathbf{q}$ scan is now found by integrating σ_{in} over E_0

$$\Delta E\sigma_{in} = \Omega B \frac{NV}{(2\pi)^3} \tag{38}$$

where we have used the normalization condition for the resolution function

$$\int R(\mathbf{q}-\mathbf{q}_0, E-E_0)\, d\mathbf{q}dE = 1 \tag{39}$$

Fig. 15 shows the phonon cross section $\frac{\Delta E}{\Omega}\sigma_{ph}$, magnon cross section $\frac{\Delta E}{\Omega}\sigma_m$ and magnetovibrational cross section $\frac{\Delta E}{\Omega}\sigma_{MV}$ for measurements near the [002] reciprocal lattice point at 90 K. The phonon cross sections shown are for the branch for which $\mathbf{e}\cdot\boldsymbol{\xi}_{q\nu} = 1$. The scattering amplitudes

$$a_M(002) = 2.16 \cdot 10^{-12}\ \text{cm}$$

$$a_N = 0.76 \cdot 10^{-12}\ \text{cm}$$

given by Steinsvoll et al.[33] have been used.

The corresponding cross sections for production of a Bragg reflected neutron group $\Delta E\sigma_B$ are easily calculated in a similar way

$$\Delta E\sigma_B = \Omega A \frac{1}{V_1} \tag{40}$$

where A is the factor multiplying the δ-functions in (13) and (14) for nuclear and magnetic scattering respectively. V_1 is to a good approximation the volume enclosed by the resolution ellipsoid in reciprocal space ($V_1 = 2.7 \cdot 10^{-4}\ \text{Å}^{-3}$ from Fig. 10).

From (40) we find the magnetic and nuclear Bragg cross sections to be

$$\frac{\Delta E}{\Omega}\sigma_B\ ((002)\ \text{magnetic}) = 1.4 \cdot 10^5\ \text{b}$$

$$\frac{\Delta E}{\Omega}\sigma_B\ ((002)\ \text{nuclear}) = 1.7 \cdot 10^4\ \text{b}$$

or four or five orders of magnitude larger than the inelastic neutron scattering cross sections, as also observed in practice.

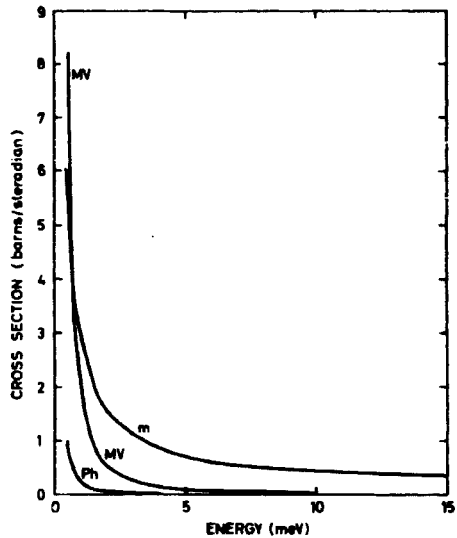

Fig. 15. Cross sections per solid angle for production of neutron groups. from magnon scattering (m), magnetovibrational scattering (MV) and phonon scattering (ph).

An exact comparison of the observed and calculated ratio of the elastic and inelastic cross sections is difficult because several large uncertain corrections must be made, such as corrections for

1) extinction arising because of non-uniform illumination of the whole sample at large cross sections
2) parasitic reflections from competitive elastic reflections by other lattice planes in the crystal
3) change in geometry taking place when the sample is not spherical, because the extinction depends on the orientation of the sample in the neutron beam.

The effect of these (and other) corrections appears to be approximately a factor of three when the intensity of the (002) nuclear Bragg reflection is compared with the intensity of a magnon neutron group at 6.5 meV.

5. Choice of Scan

Since the energy of an excitation $\varepsilon_j(\mathbf{q})$ only depends on the wavevector of the excitation $\mathbf{q} = \mathbf{k}_1 - \mathbf{k}_2 - \boldsymbol{\tau}$, there are several scans in which the same branch of the dispersion relation can be measured.

(a) Creation or absorption of the excitations can be employed.

(b) Constant E or constant $\mathbf{q}$ scans can be used.

(c) In constant $\mathbf{q}$ scans, the energy of either the incident or scattered neutrons can be fixed ($\mathbf{k}_1$ constant or $\mathbf{k}_2$ constant).

(d) The value of the fixed energy (in both constant E and constant $\mathbf{q}$ scans) can be chosen.

(e) The $\boldsymbol{\tau}$-vector can be chosen.

(f) There may be a choice between several symmetrically equivalent directions in the sample crystal.

Although such equivalent scans give the same dispersion relation, the quality of the observed neutron group may be very *different* for the *different* scans. Since the inelastic scattering cross sections are small, and counting times therefore long, it is extremely important to choose the best scans. We will therefore discuss how to choose the scan in order to optimize the intensity, width and shape of the neutron groups, and background conditions.

(a) Creation or absorption scans

The magnon creation cross section is proportional to $n_j(\mathbf{q}) + 1$, where the population factor $n_j(\mathbf{q})$ is

$$n_j(\mathbf{q}) = \left[\exp\frac{\varepsilon_j(\mathbf{q})}{kT} - 1\right]^{-1}$$

whereas the magnon absorption cross section is proportional to $n_j(\mathbf{q})$. For $\varepsilon_j(\mathbf{q}) \gtrsim kT$, which condition was generally satisfied in these experiments, $n_j(\mathbf{q}) < 1$ and magnon creation gives an appreciably larger intensity. Magnon creation was therefore used in all cases.

(b) Constant E or constant $\mathbf{q}$ scans

Whether a constant E or constant $\mathbf{q}$ scan gives a narrower neutron group depends on the slope of the resolution ellipsoid relative to the slope of the dispersion relation. If the dispersion relation is very steep, a constant E scan is better, while constant $\mathbf{q}$ scans give the better results for the flat parts of the dispersion relation.

For very small energy transfers, the constant E scan gives a more constant

background, since the part of the background originating from incoherent scattering depends strongly on the energy transfer at which the spectrometer is set.

Both constant E and constant **q** scans were therefore used.

(c) Fixed $|\mathbf{k}_1|$ or fixed $|\mathbf{k}_2|$

The monochromatic neutron beam intensity and the efficiency of the analyzer depend on the incoming and scattered neutron energies respectively. This dependence of the intensity of the scattered neutrons on the incoming and scattered neutron energies can, however, be avoided by fixing the energy of the scattered neutrons (so that the efficiency of the analyzer is constant) and determining the counting time by a thin monitor counter in the monochromatic neutron beam The inverse velocity dependence of the monitor counter cancels the $\frac{1}{k_1}$ dependence of the cross section[28].

This means that the neutron groups will be symmetric and that their relative intensity can be calculated from the cross section, without corrections for the changes of the monochromatic neutron beam intensity and the efficiency of the analyzer.

Furthermore, since the scattering angle in the analyzer in this case is constant, it is possible to shield the analyzer very efficiently, and this was found to be extremely important in reducing background.

For these reasons, fixed scattered neutron energy was used in all measurements.

(d) Choice of the fixed energy of the scattered neutrons

The monochromatic neutron intensity as a function of neutron energy is shown in Fig. 16. The range of magnon energies is from 0 meV to about 15 meV. Since we have fixed the scattered neutron energy, it means that, in an experiment with neutron energy loss, we use monochromatic neutrons in the range from the fixed scattered neutron energy to about 15 meV higher.

To optimize intensity this energy range should be chosen around the peak of the distribution in Fig. 16. However the resolution of the spectrometer is best at low neutron energies.

As a compromise, a scattered neutron energy of 18.6 meV vas generally chosen. For a typical magnon we then use neutrons of incident energy around 25 meV. At this energy we have half of the maximum intensity at 50 meV but the width of the neutron groups is also smaller than it would be at 50 meV.

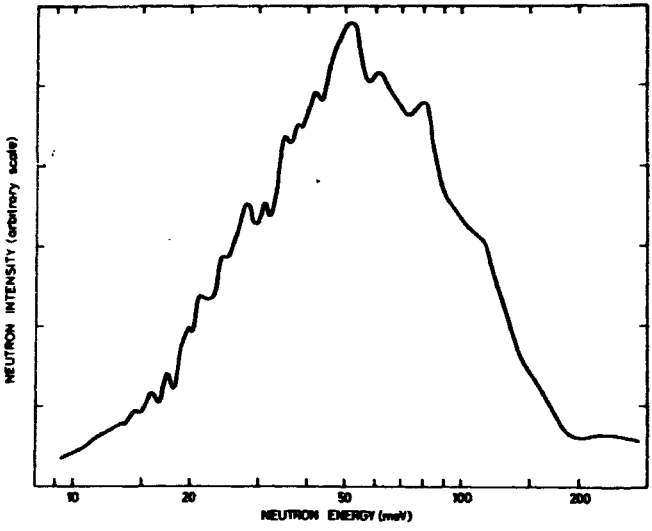

Fig. 16. Intensity of first order neutrons from the monochromator, as a function of neutron energy measured with the use of a quartz filter[34]. The spikes are due to parasitic reflections in the monochromator crystal.

(From (30) it is seen that the energy resolution of the monochromator system is proportional to $E_i \cot \theta_M \approx E_i^{3/2}$). The peak count rate is therefore about the same but a sharper peak is observed.

At still lower neutron energies the peak count rate begins to decrease. In a few cases where extreme resolution was necessary, namely for very small energy transfers, a scattered neutron energy of 10 meV was used, in order to separate the magnon peak from the elastic peak, and in order to measure the widths of the magnon neutron groups.

A better resolution can also be obtained by better collimation. The collimations used at 18.6 and 10 meV were respectively 30', 40', 20', 25' and 30', 25', 15', 15' counted from the reactor outwards. To increase these collimations further would result in loss of neutron intensity because of the thickness of the plates of the Soller collimators and the decrease of the solid angle of scatter-

ing, and furthermore would not improve the vertical resolution, in contrast to the situation when the neutron energy is lowered.

(e) Choice of τ-vector

Since the magnetic scattering amplitude $a_M(\varkappa)$ is a strongly decreasing function of $\varkappa$, it is necessary to choose reciprocal lattice vectors τ with low Miller indices.

In addition the geometrical structure factor $F(\varkappa)$ depends on the choice of τ. As seen from (27) the geometrical structure factor is a continuous function of $\varkappa$. For the three reciprocal lattice points of lowest Miller indices, the geometrical structure factor for acoustic and optical magnons calculated from (27) is given in Table I.

τ	$F_a(\varkappa = \tau)$	$F_o(\varkappa = \tau)$
[100]	1/2	3/2
[110]	2	0
[002]	2	0

TABLE I

Geometrical structure factors for inelastic neutron scattering

Scans around [100] were therefore used to measure the optical branches, whereas the acoustic branches were measured in scans around [110] and [002].

(f) Choice between equivalent directions

The direction of the magnon wavevector q relative to τ is very important for the width of the neutron groups, and scans in directions for which focusing is obtained should be chosen if possible. From Fig. 10 it is seen that the width in a focusing scan may be an order of magnitude less than the width in a defocusing scan, the integrated intensity being the same.

From Fig. 15 it is seen that the magnetovibrational and phonon cross sections increase faster than the magnon cross section with decreasing energy. At low energies the phonon peaks may therefore disturb the measurement of the magnons, if they fall at about the same energies. By choosing a scan for which $|e \cdot \delta_{q_j}|^2 = 0$ for the disturbing branch, it is however possible to eliminate the disturbing peak.

6. Disturbing Peaks

Peaks in the scattered neutron intensity may arise from other sources than one magnon and one phonon scattering, and may therefore disturb the measurements seriously. Such peaks arise from neutrons which have been scattered in the monochromator, sample and analyzer before being counted. Because the inelastic neutron scattering cross sections are small (4 or 5 orders of magnitude smaller than elastic cross sections), Bragg scattering in two of the three crystals is sufficient to produce a peak of the same magnitude as a magnon or phonon peak. Examples of such spurious peaks are

(1) Bragg scattering in the monochromator and analyzer, and incoherent elastic scattering in the sample.

Since higher order Bragg reflections take place, peaks due to these processes will be observed whenever

$$n_1 E_1^2 = n_2^2 E_2$$

$n_1 = 1, 2, 3 \ldots$ and $n_2 = 1, 2, 3 \ldots$ are the order of reflection and E_1 and E_2 are the first order energies of the monochromator and analyzer respectively. For $E_2 = 18.6$ meV, peaks in the scatfered neutron intensity will therefore be seen for energy transfers 0 meV (1 order in monochromator and 1 order in analyzer) 25.25 meV (2 order in monochromator and 3 order in analyzer) 55.8 meV (1 order in monochromator and 2 order in analyzer).

Reflections of higher than 3 order are weak because there are few neutrons of such a high energy (see Fig. 16).

Since the magnon energies range from 1–15 meV, only the peak at 0 meV may be disturbing. However, if constant E scans are used for low energy transfer measurements, the background from this process is constant.

(2) Bragg scattering in the monochromator and analyzer and Bragg scattering in the sample, seen for "inelastic" settings of the spectrometer due to the shape of the resolution function.

Fig. 17 illustrates how they arise in a focusing constant **q** scan.

In this scan the resolution ellipsoid is moved on the vertical line shown. When the extension of the major axis of the resolution ellipsoid goes through $\mathbf{q} = 0, E = 0$ a peak in the scattered neutron intensity will be observed due to elastic scattering. Since this peak will arise for "inelastic settings" of the spectrometer it might be mistaken for a magnon reflection. Its intensity will depend on E_m, being larger at lower energies, just as the magnon re-

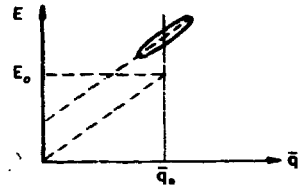

Fig. 17. Diagram showing how spurious peaks in the scattered neutron intensity may arise when the extention of the major axis of the resolution ellipsoid goes through $\mathbf{q} = 0, E = 0$.

flections would be (due to the population factor). It will give rise to a spurious linear "dispersion curve". It will not, however, arise in non-focusing or defocusing scans. In several cases, these spurious reflections ruined a focusing scan because they were not separated from the magnon reflections, so that a non-focusing scan had to be used. For instance, all measurements of the dispersion relation in the c-direction were performed with non-focusing scans.

(3) Bragg scattering in the monochromator, incoherent elastic scattering in the analyzer (or vice versa) and Bragg scattering in polycrystalline material around the sample.

These peaks arise when the scattering angle and incident (or scattered) neutron energy are such that the Bragg Law is satisfied for a set of planes in the polycrystalline material around the sample. Since they only occur for combinations of scattering angle and neutron energy determined by the distance between the planes in the polycrystalline material, they can be readily identified. They can be avoided by changing to a scan where such combinations of scattering angle and neutron energy do not occur in the region of the magnon neutron group.

(4) Second order Bragg reflections in monochromator and analyzer and magnon or phonon scattering in the sample.

The magnon or phonon excited will have wavevector $2\mathbf{q}_1$, where $\mathbf{q}_1$ is the wavevector the spectrometer is set to excite in first order (see Fig. 18).

Its energy will be E_2 (from the dispersion relation), but it will be seen for an energy setting of the spectrometer of $\frac{1}{4} E_2$. As a result it will give rise to a peak in the scattered neutron intensity which generally will fall at lower

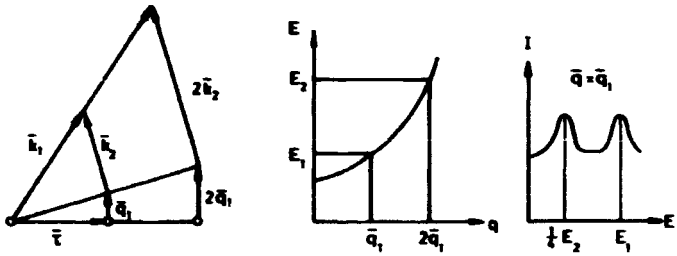

Fig. 18. Diagram showing how second order neutrons may produce a spurious peak in the scattered neutron intensity, generally at lower energies than the one arising from first order reflections.

energies than the wanted peak, and therefore not disturb the measurement. Second order neutrons can be removed by neutron filters, or higher energy neutrons can be used. As shown in Fig. 19 the second order fraction decreases strongly with increasing neutron energy.

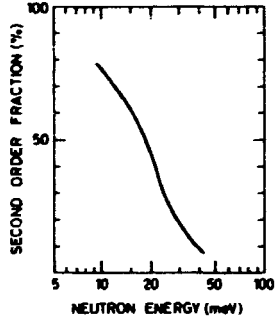

Fig. 19. Second order fraction of neutrons in the monochromatic neutron beam, measured with the use of a quartz filter.

First order Bragg reflection in the monochromator and second order Bragg reflections in the analyzer (or vice versa) leads to energy transfers much larger than the magnon energies and will therefore not produce disturbing peaks.

Because of the possibility of such spurious peaks and also to check the consistency of the measurements, all branches of the dispersion relation were checked using at least two geometrically different scans.

III. Results and their Interpretation

This chapter gives the results of measurements of inelastic neutron scattering from Tb and Tb-10% Ho, and the interpretation of these results in terms of the magnetic interactions in rare earth metals.

Tb was chosen for these experiments because it is one of the few rare earth metals which does not have a very high thermal neutron absorption cross section, so that a sufficient intensity of inelastically scattered neutrons can be obtained to give satisfactory information on the magnon dispersion relations. Further, since the properties of Tb are typical of those of the heavy rare earth metals, it is hoped that a careful investigation of the magnetic excitations may give information on the whole series of rare earth metals. For measurements in the spiral temperature region, an alloy of Tb-10% Ho gave better experimental results, because the addition of 10% Ho to Tb increases the tendency towards spiral ordering and makes the spiral structure stable over a larger temperature region (For Tb: $T_C = 216$ K, $T_N = 226$ K and for Tb-10% Ho. $T_C = 195$ K, $T_N = 220$ K).

The measurements of the dispersion relation in ferromagnetic Tb are first described. Fourier transformed exchange parameters and interplanar exchange parameters are derived from these measurements. From measurements of the temperature dependence of the magnon energies in ferromagnetic terbium it is shown that the exchange forces scale roughly as the ordered moment, in accordance with the random phase approximation. The Fourier transformed exchange parameter $J(\mathbf{q})$ for Tb-10% Ho in the spiral phase is found to have two maxima for $\mathbf{q} = \mathbf{Q}$ (the wavevector of the spiral) and $\mathbf{q} = \tau - \mathbf{Q}$. The former of these peaks is responsible for the stability of the spiral structure. The Fourier transformed exchange parameter is related to the Fermi surface, and the abrupt flattening of the peak in $J(\mathbf{q})$ at the ferromagnetic transition is ascribed to the splitting of the different spin bands by the ferromagnetic exchange interaction. From measurements of the width of the inelastically scattered neutron groups in the ferromagnetic phase as a function of temperature and magnon wavevector, it is shown that the magnon lifetimes are primarily determined by their interaction with the conduction electrons. A rapid decrease in the width observed at low magnon wavevectors is ascribed to the splitting of the spin-up and spin-down Fermi surfaces in the ferro-

magnetic phase. Finally the observations of a magnon-phonon interaction and of a resonant magnon mode are described.

Short reports on these measurements have been published[35, 36]. A more detailed treatment will be given here.

1. Dispersion Relation for Magnons in Tb at 90° K

The magnon dispersion relations for Tb at 90° K along all the symmetry lines in the Brillouin zone are shown in Fig. 20. Most of the observed neutron groups are well defined with a peak intensity of typically 10 counts per min. and a background of 2 counts per min. From the accuracy in determining the center of the neutron groups and the spread of these obtained in different scans (indicated by different symbols on Fig. 20), the uncertainty of the measured magnon energies is estimated to be ± 0.1 meV.

A degeneracy of the acoustic and optical branches of the dispersion relation is observed along the line K-H. Such degeneracies can be predicted by group theoretical arguments[37, 38] using the magnetic space group, which takes into account the symmetry of the Hamiltonian. Assuming the Hamiltonian (7), with isotropic exchange, the observed degeneracy is consistent with the group theoretical arguments. This Hamiltonian, which is the simplest which can account for the magnetic structure of the rare earth metals, is used in interpreting all the experimental results.

With this Hamiltonian, the dispersion relation in the ferromagnetic phase for an arbitrary direction is[17]

$$\varepsilon_\lambda(\mathbf{q}) = J\left\{f_\lambda^2 + 2(B + 21GJ^4)f_\lambda + 72GJ^4(B + 3GJ^4)\right\}^{1/2} \qquad \lambda = 1,2 \quad (43)$$

where

$$f_\lambda(\mathbf{q}) = J(0) - J(\mathbf{q}) + J'(0) + (-1)^\lambda |J'(\mathbf{q})| \qquad (44)$$

The values 1 and 2 of the subscript λ refer to the acoustic and optical branch, respectively.

We have introduced two Fourier transformed exchange parameters

$$J(\mathbf{q}) = \sum_{\mathbf{R}_l} J(\mathbf{R}_l)\, e^{i\mathbf{q}\cdot\mathbf{R}_l}$$

$$J'(\mathbf{q}) = \sum_{\mathbf{R}_{l'}} J(\mathbf{R}_{l'})\, e^{i\mathbf{q}\cdot\mathbf{R}_{l'}} \qquad (45)$$

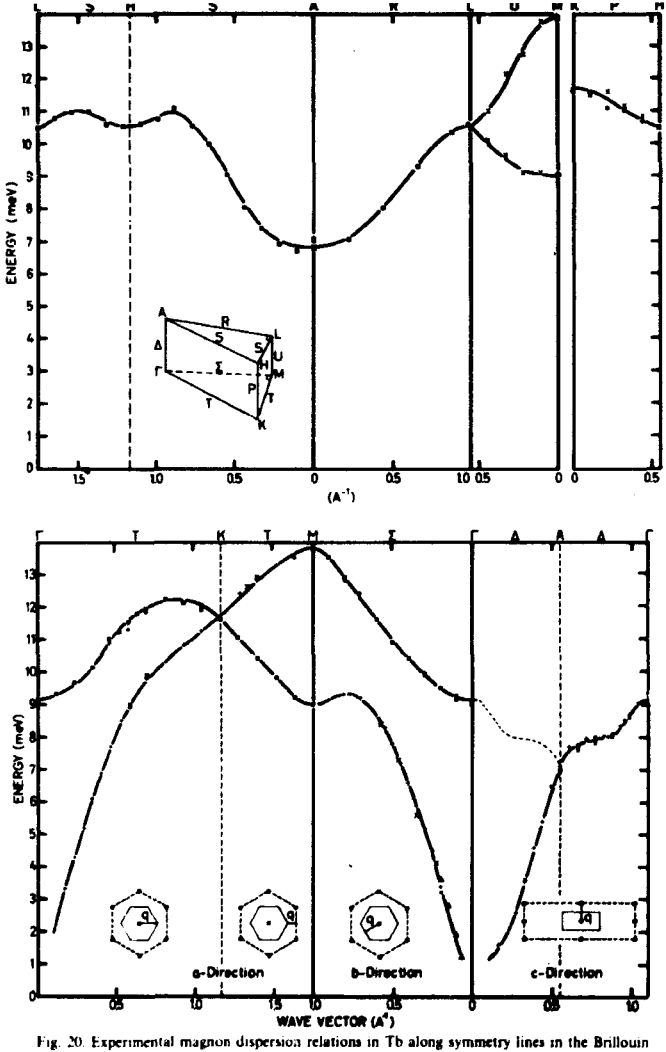

Fig. 20. Experimental magnon dispersion relations in Tb along symmetry lines in the Brillouin zone at 90°K.

where the sums in (45) are over all vectors from one atom to other atoms in the same sublattice ($\mathbf{R}_1$) and over all vectors to atoms in the other sublattice ($\mathbf{R}_{1'}$) respectively.

From (43) we find

$$f_1(\mathbf{q}) = \sqrt{\left(\frac{f_2(\mathbf{q})}{J}\right)^2 + (B-15GJ^4)^2} - (B+21GJ^4) \tag{46}$$

(the other solution, with a minus sign on the square root, is seen to be false, since it cannot give $f_1(0) = 0$ with positive B and G)

From (44) we get

$$\begin{aligned} J(0) - J(\mathbf{q}) &= \tfrac{1}{2}\left\{f_1(\mathbf{q}) + f_2(\mathbf{q}) - f_2(0)\right\} \\ J'(0) - |J'(\mathbf{q})| &= \tfrac{1}{2}\left\{f_1(\mathbf{q}) - f_2(\mathbf{q}) + f_2(0)\right\} \\ J'(0) + |J'(\mathbf{q})| &= \tfrac{1}{2}\left\{-f_1(\mathbf{q}) + f_2(\mathbf{q}) + f_2(0)\right\} \end{aligned} \tag{47}$$

The c-direction has a particularly high symmetry. For this direction the atoms of the two sublattices form alternate planes perpendicular to the c-direction, separated by the distance $\frac{1}{2}c$.

Since further $J'(\mathbf{q}) \geq 0$ for $0 \leq q \leq \dfrac{\pi}{c}$

and $J'(\mathbf{q}) \leq 0$ for $\dfrac{\pi}{c} \leq q \leq \dfrac{2\pi}{c}$

we find

$$\begin{aligned} f_1(\mathbf{q}) &= J(0) - J(\mathbf{q}) + J'(0) - |J'(\mathbf{q})| = J(0) + J'(0) - J(\mathbf{q}) - J'(\mathbf{q}) \qquad 0 \leq q \leq \frac{\pi}{c} \\ f_2(\mathbf{q}) &= J(0) - J(\mathbf{q}) + J'(0) + |J'(\mathbf{q})| = J(0) + J'(0) - J(\mathbf{q}) - J'(\mathbf{q}) \qquad \frac{\pi}{c} \leq q \leq \frac{2\pi}{c} \end{aligned} \tag{48}$$

so that the dispersion relations for the c-direction can be regarded as a single acoustic branch extending twice as far as the first Brillouin zone boundary, if

the points of the optical branch are moved from $\mathbf{q}$ to $\frac{2\pi}{c} - \mathbf{q}$. If this rearrangement is carried out, we get from (45)

$$J(0) - J^c(\mathbf{q}) \quad 2 \sum_{m=1}^{\infty} J_m^c (1 - \cos^{1}{}_{2} mcq) \qquad (-\frac{2\pi}{c} \le q \le \frac{2\pi}{c}) \tag{49}$$

so by Fourier inversion of $J(0) - J^c(\mathbf{q})$, it is possible to determine the interplanar exchange parameter J_m^c (m odd gives interplanar exchange parameters between planes in different sublattices).

Also for the a-direction $J^a(\mathbf{q})$ is real, but all planes perpendicular to the a-direction contain atoms of both sublattices, so we cannot consider the dispersion relation as a single acoustic branch, in contrast to the c-direction.

From (45) we get for the a-direction

$$J(0) - J^a(\mathbf{q}) \quad 2 \sum_{m=1}^{\infty} J_m^a (1 - \cos^{1}{}_{2} maq) \qquad (-\frac{2\pi}{a} \le q \le \frac{2\pi}{a})$$

$$J^a(0) - J^a(\mathbf{q}) \quad 2 \sum_{m=1}^{\infty} J_m^a (1 - \cos^{1}{}_{2} maq) \qquad (-\frac{2\pi}{a} \le q \le \frac{2\pi}{a}) \tag{50}$$

For the b-direction $J^b(\mathbf{q})$ is complex and we get from (45)

$$J(0) - J^b(\mathbf{q}) \quad 2 \sum_{m=1}^{\infty} J_m^b (1 - \cos \frac{\sqrt{3}}{2} maq) \qquad \left(-\frac{2\pi}{\sqrt{3}a} \le q \le \frac{2\pi}{\sqrt{3}a}\right)$$

$$J^b(0) - J^b(\mathbf{q}) = \sum_{p=1}^{\infty} J_p^b (1 - \cos \frac{\sqrt{3}}{2} paq) \left(-\frac{2\pi}{\sqrt{3}a} \le q \le \frac{2\pi}{\sqrt{3}a}\right) \tag{51}$$

where

$$J_p^b = 2 \sum_{m=-\infty}^{\infty} J_m^b J_{m+p}^b$$

From measurements of the dispersion relation $\varepsilon_i(\mathbf{q})$ it is thus possible to determine the Fourier transformed exchange parameters from (46) and (47) if the anisotropy constants B and G are known. Having determined the Fourier transformed exchange parameters, it is then possible using (49), (50) and (51) to determine the interplanar exchange parameters.

The two-fold crystal field anisotropy constant B was determined from the $\mathbf{q}$-dependence of the neutron group intensities for the Tb-10% Ho crystal at 110 K. (The alloy was used rather than pure Tb because it was considerably larger, and therefore gave higher neutron group intensities. The addition of 10% Ho to Tb was assumed not to change the anisotropy significantly). Lindgard et al. [19] have shown that there is an additional factor

$$n = \sqrt{1 - \left(\frac{JB}{\varepsilon(\mathbf{q})}\right)^2} = \frac{JB}{\varepsilon(\mathbf{q})} \tag{52}$$

in the formula for the magnon cross section (19) if two-fold anisotropy is taken into account. The intensities of the neutron groups therefore increase faster than $n_i(\mathbf{q}) = 1$ as the magnon energies decrease. Fig. 21 shows how this is used to determine B. The integrated intensities are rather uncertain, particularly for low magnon energies where the background subtraction is difficult, because of large contribution to the background from the elastic reflection. Considering this, the values of the two fold anisotropy are remarkably consistent. The average value, $B = 0.25$ meV/ion, was therefore chosen. The fact that the $\mathbf{q}$-dependence of the intensity agrees so well with calculations assuming Heisenberg exchange and two- and six-fold single ion crystal field anisotropy, indicates that the anisotropy of the exchange interaction is small.

From the expression for the dispersion relation (43) it is seen that the acoustic branch does not go to zero for $\mathbf{q} = 0$. There is an energy gap $J\Delta$ of the size

$$J\Delta = J\sqrt{72GJ^4(B + 3GJ^4)} \tag{53}$$

For Tb-10% Ho an energy gap of 0.75 meV was observed at 110 K (see later). This value for the energy gap together with $B = 0.25$ meV/ion gives from (53) that $GJ^4 = 8.7 \cdot 10^{-4}$ meV/ion at 110 K. The two-fold anisotropy

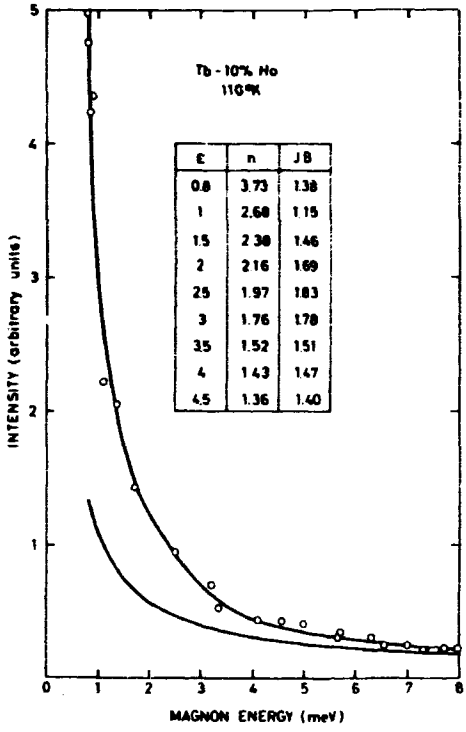

Fig. 21. Determination of the two-fold anisotropy parameter from the intensities of the inelastically scattered neutron groups. n is the ratio of the observed integrated intensity (the upper curve) and $n_q(\omega) + 1$ (the lower curve) calculated from (25).

constant B is in fair agreement with torque measurements of Rhyne and Clark[19] who find B ≈ 0.33 meV/ion at 110 K for Tb. Our six-fold anisotropy constant, however, is much larger than the value Rhyne and Clark deduce from magnetostriction measurement (a factor of six larger). This comparison is based on

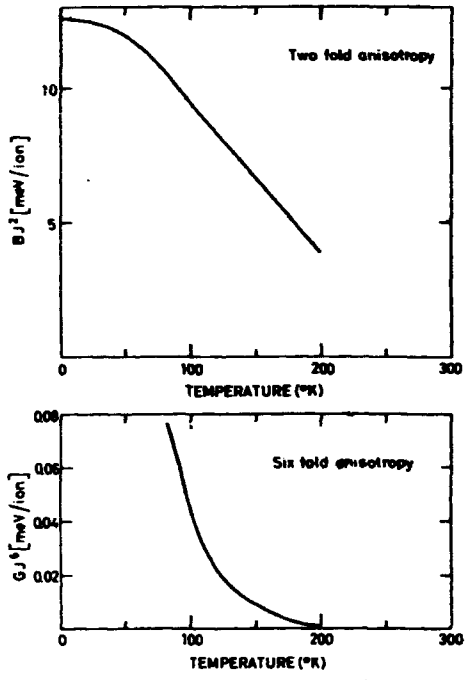

Fig. 22. Temperature dependence of the anisotropy parameters, obtained from magnetization measurements of Rhyne and Clark[35], but normalized to our neutron results at 110 K.

the classical relations[17] between the macroscopic and microscopic anisotropy parameters

$$K_2 \simeq \frac{2}{3} BJ^2 \qquad K_6^6 \simeq GJ^6$$

A quantum mechanical treatment of the macroscopic anisotropy parameters[40], taking into account the dependence of the zero-point magnon

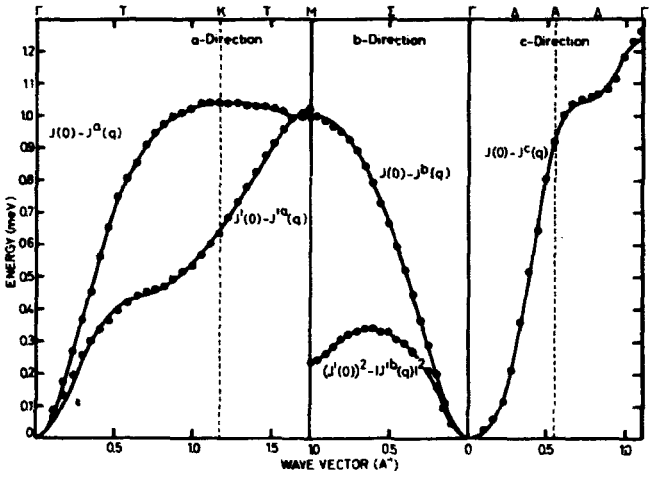

Fig. 23. Fourier transformed exchange parameters for Tb at 90 K.

energy on magnetization, substantially modifies both relations, however, and this may account for the discrepancy. In interpreting our results, we have used the anisotropy constants derived from our neutron measurements at 110 K, but scaled with temperature according to the results of Rhyne and Clark[19]. The temperature dependence of the anisotropy constants determined in this way is shown in Fig. 22.

Fig. 23 shows the Fourier transformed exchange parameters. The points are calculated from average values of the measured magnon energies (Fig. 20) using (46) and (47) and the anisotropy constants in Fig. 22.

The accuracy of these points depends on the accuracy of the experimental *dispersion relation*, the accuracy of the measured energy gap, and the uncertainty of the estimated two-fold anisotropy B.

For simplicity let us consider the determination of $J(0)-J(\mathbf{q})$ for the c-direction in the ferromagnetic phase. From (43) we find

	a-direction	b-direction	c-direction
J_1	0.200	0.240	0.305
J_2	0.120	0.040	0.075
J_3	0.045	0.010	0.005
J_4	0.020	0.005	−0.035
J_5	0.005		
J_1'	0.195	0.050	
J_2'	−0.005	0.050	
J_3'	0.050	0.010	
J_4'	0.015	0.010	
J_5'	0.010		

TABLE II

Interplanar exchange parameters.
All are given in meV except the J' for the b-direction, which are in meV^2. Accuracy ± 0.005 meV

$$J(0) - J(q) \quad f(q) \cong \sqrt{\left(\frac{\varepsilon(q)}{J}\right)^2 \cdot B^2 - \Delta^2} - B \tag{54}$$

since $B >> 21GJ^4$.

From (54) we find

$$\frac{df(q)}{d\varepsilon(q)} \frac{1}{J} \frac{\frac{\varepsilon(q)}{J}}{\sqrt{\left(\frac{\varepsilon(q)}{J}\right)^2 \cdot B^2 - \Delta^2}} < \frac{1}{J} \frac{1}{6}$$

so that the uncertainty of ± 0.1 meV in the measurement of $\varepsilon(q)$ introduces an uncertainty of less than ± 0.02 meV in the determination of $J(0) - J(q)$.

Differentiating (54) with respect to Δ we find

$$\frac{df(q)}{d\Delta} \frac{\Delta}{f(q) \cdot B} < \frac{\Delta}{B} \frac{0.75}{6 \cdot 0.25} 0.5$$

With an uncertainty of ± 0.1 meV in the determination of the energy gap J Δ we therefore get an uncertainty of less than $\pm 0.5 \cdot \frac{1}{6} \cdot 0.1 \cong \pm 0.01$ meV in the determination of J(0) – J(q).

Finally we differentiate with respect to B and find

$$\frac{df(q)}{dB} \Big/ \frac{f(q)}{f(q) - B} < \frac{1.2}{1.2 - 0.25} \sim 0.8$$

B can therefore deviate $\pm \frac{0.02}{0.8} = \pm 0.025$ meV, or $\pm 10\%$ from the value used without introducing additional uncertainty in the determination of J(0) – J(q).

Fig. 23 also shows a least-squares fit of expressions (49), (50) and (51) to the data, and the interplanar exchange parameters thus obtained are given in Table II.

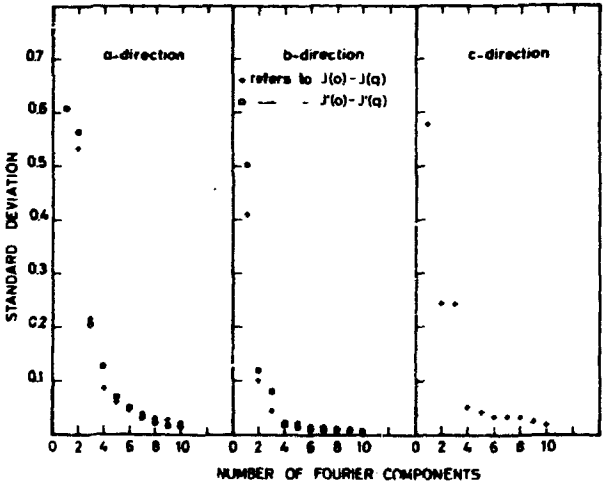

Fig. 24. Standard deviation versus number of Fourier components of J(0) - J(q) used to fit the experimental data

Fig. 24 shows the standard deviation of the least-squares fit as a function of the number of Fourier components (interplanar exchange parameters). It is seen that after four or five Fourier components, the standard deviation does not change significantly. This number of interplanar exchange parameters therefore fits the data within the experimental accuracy.

It is seen that the exchange interaction is long range (reaches at least 5 planes away) and oscillatory (some of the interplanar exchange constants are negative), as expected from an indirect exchange interaction.

The oscillatory long range nature of the interaction is also seen from the "interlinear" exchange parameters and "interatomic" exchange parameters calculated from our experimental measurements by Stringfellow and Windsor[41] and Goodings[42], respectively.

It should be noted that $J(0) - J(q)$ for the c-direction is everywhere positive, which satisfies the sufficient condition for stability of the ferromagnetic structure.

2. Temperature Dependence of Magnon Energies in Tb

The results of measurements of the dispersion relation for magnons propagating in the c-direction are shown in Fig. 25 for four temperatures in the ferromagnetic phase of Tb.

The magnon energies are seen to decrease with increasing temperature. The most important effect contributing to this temperature dependence is probably due to interactions among spin waves. The effect of these interactions on the spin wave energies is often referred to as spin wave renormalization. This effect simply results from the fact that, when there is a sufficient number of spin waves present to cause an appreciable misalignment of the spins, it takes less energy to create a spin wave than when there are few waves present[43].

It is useful to distinguish between those interactions originating in the exchange terms and those from the crystal field terms of the Hamiltonian, referring to the corresponding effects as exchange renormalization and crystal field renormalization.

Brooks et al.[44] have shown that the effect of crystal field renormalization is to introduce a temperature dependence of the crystal field anisotropy parameters similar to that shown in Fig. 22.

The effect of exchange renormalization can therefore be found by comparing the Fourier transformed exchange parameters obtained from the experimental dispersion relation, using (8), and the crystal field parameters from Fig. 22.

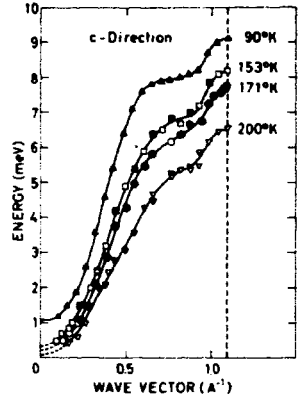

Fig. 25. Temperature dependence of magnon energies in the c-direction in the ferromagnetic phase of Tb.

This is done in Fig. 26(a), from which it is seen that the effect of the exchange renormalization is to weaken the exchange interaction. This is in qualitative agreement with theoretical predictions[43,45] according to which the effective exchange parameters should scale as the ordered moment in the high temperature limit (where the random phase approximation is valid). Fig. 26(b) therefore shows the Fourier transformed exchange parameters from 26(a) divided by the ordered moment $<J_z>$. The ordered moment was taken from neutron diffraction measurements of Dietrich and Als-Nielsen[46]. There is an approximate proportionality between the exchange constants and the moment, but the detailed form of $J(\mathbf{q})$ changes with temperature, and this reflects the change in energy band structure with ordering, as well as the limitations of the theory.

At all the temperatures, $J(0) - J(\mathbf{q})$ is seen to have no other minimum than for $\mathbf{q} = 0$, and this is consistent with the fact that the ferromagnetic structure is stable. It is, however, in disagreement with those theories[15] which assume a maximum of $J(0) - J(\mathbf{q})$ at $\mathbf{q} = \mathbf{Q}$ for all temperatures, and explain the stability of the ferromagnetic structure at low temperatures by the effect of the strongly temperature-dependent six-fold anisotropy.

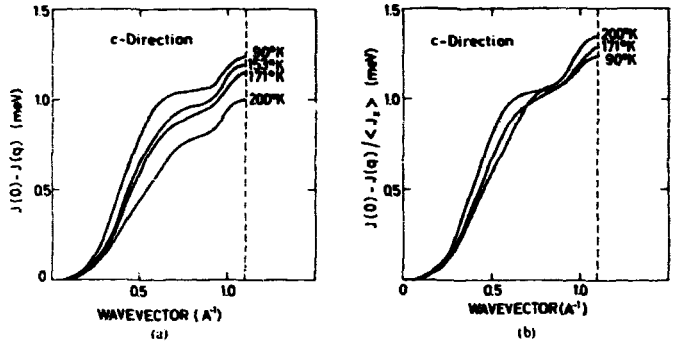

Fig. 26. (a) Temperature dependence of the Fourier transformed exchange parameters in the c-direction in the ferromagnetic phase of Tb.
(b) $J(0) - J(q)$ divided by the ordered moment in the ferromagnetic phase of Tb.

3. Magnons in the Spiral Phase of Tb-10% Ho

As seen from the magnon cross section formula (20) for the spiral structure, in general three inelastic neutron groups are observed in constant q or constant E scans in the spiral phase. In constant E scans they are separated by the distance Q, the wavevector of the spiral. By choosing scans in which the scattering vector is parallel to the c-axis it is possible to eliminate the middle peak, making the resolution of the remaining two peaks easier.

Such scans were used to measure the magnon dispersion relation in the spiral phase. Fig. 27 shows the results of a constant E scan for Tb-10% Ho at 200 K. The double peak observed can easily be decomposed into two peaks, separated by the correct distance ($2Q = 0.278$ Å^{-1}). The wavevector of the spiral Q is known very accurately from the position of the magnetic Bragg reflections which, as seen from (15), fall as satelites on the nuclear Bragg reflection at a distance $\pm Q$.

The dispersion relation shown in Fig. 28(a) is obtained from a series of such constant E scans. *The points are those experimentally measured and the solid* curve is the least squares fit of expression (9) to the experimental points, taking six Fourier components of $J(0) - J(q)$. In the least squares fit, the various experimental points have been weighted according to the accuracy of the

18. B. R. Cooper, R. J. Elliott, S. J. Nettel and H. Suhl
Phys. Rev. **127** 57 (1962).
19. P. A. Lindgård, A. Kowalska and P. Laut
J. Phys. Chem. Solids **28**, 1357 (1967).
20. R. Weinstock
Phys. Rev. **65**, 1 (1944).
21. O. Halpern and M. H. Johnson
Phys. Rev. **55**, 898 (1939).
22. E Fermi
Ricerca Scient. **7**, Part 2, 13 (1936).
23. Yu. A. Izyumov
Soviet Physics USPEKHI **16**, 359 (1963).
24. W. M. Lomer and G. Low
In Thermal Neutron Scattering (Ed. P. A. Egelstaff)
Academic Press, London (1965).
25. V. G. Bar'yaktar and S. V. Maleev
Soviet Physics – Solid State **5**, 858 (1963).
26. G. Low
Proc. Phys. Soc. **79**, 473 (1962).
27. W. L. Bragg
Proc. Cambridge Phil. Soc. **17**, 43 (1913).
28. B. N. Brockhouse
In Inelastic Scattering of Neutrons, p. 113 (IAEA, Vienna, 1961).
29. M. F. Collins
Brit. J. Appl. Phys. **14**, 805 (1963).
and Brit. J. Appl. Phys. **17**, 147 (1966) corrigendum
30. R. Stedman and G. Nilsson
Inelastic Scattering of Neutrons Vol. I, p. 211, (IAEA, Vienna, 1965).
31. G. E. Peckham, D. H. Saunderson and R. I. Sharp
Brit. J. Appl. Phys. **18**, 473 (1967).
32. J. Bergsma and C. van Dijk
Reactor Centrum Nederland Rep., RCN-36 (1965).
33. O. Steinsvoll, G. Shirane, R. Nathans, M. Blume, H. A. Alperin
and S. J. Pickart
Phys. Rev. **161**, 499 (1967).
34. H. Bjerrum Møller, F. J. Shore and V. L. Sailor
Rev. Sci. Instr. **32**, 654 (1961).
35. H. Bjerrum Møller and J. C. Gylden Houmann
Phys. Rev. Letters **16**, 737 (1966).

36. H. Bjerrum Møller, J. C. Gylden Houmann and A. R. Mackintosh
Phys. Rev. Letters **19**, 312 (1967).
37. W. Brinkman
J. Appl. Phys. **38**, 939 (1967).
38. W. Brinkman and R. J. Elliott
Proc. Roy. Soc. (to be published).
39. J. J. Rhyne and A. E. Clark
J. Appl. Phys. **38**, 1379 (1967).
40. G. Johansen and J. R. Schrieffer
(private communication).
41. M. W. Stringfellow and C. G. Windsor
Proc. Phys. Soc. (to be published).
42. D. A. Goodings
(to be published).
43. F. Keffer and R. Loudon
J. Appl. Phys. **32**, 2 S (1961).
44. M. S. S. Brooks, D. A. Goodings and H. I. Ralph
(to be published).
45. S. V. Tyablikov.
Ukr. Math. Zh. **11**, 287 (1959).
H. B. Callen,
Phys. Rev. **130**, 890 (1963).
46. O. W. Dietrich and J. Als-Nielsen
Phys. Rev. **162**, 315 (1967).
47. R. J. Elliott and H. Stern
In Inelastic Scattering of Neutrons, p. 61 (IAEA. Vienna, 1961).
48. A. H. Luther and T. Tanaka
(to be published).
49. T. Wolfram and J. Callaway
Phys. Rev. **130**, 2207 (1963).
50. H. Bjerrum Møller and A. R. Mackintosh
Phys. Rev. Letters **15**, 623 (1965).
51. E. C. Svensson and B. N. Brockhouse
Phys. Rev. Letters **18**, 858 (1967).
52. C. Kittel
Quantum Theory of Solids, p. 74, John Wiley and Son, New York, London (1963).
53. G. Dolling and R. A. Cowley
Phys. Rev. Letters **16**, 683 (1966).

Dansk resumé
af
Magnoner i sjældne jordarter undersøgt ved hjælp af uelastisk neutronspredning.

Den foreliggende rapport beskriver en eksperimentel undersøgelse af de magnetiske vekselvirkninger i Tb og i en 90% Tb–10% Ho legering ved hjælp af uelastisk neutronspredning.

I indledningen gives en beskrivelse af de relevante dele af teorien for magnetisme i sjældne jordarter. Desuden omtales de forskellige typer af neutronspredning, som kan forekomme.

Kapitel II behandler den eksperimentelle teknik. Først beskrives Risø's tre-akse-spektrometer, som blev anvendt til målingerne. Dernæst vises det, at den eksperimentelle opløsningsfunktion kan måles, og at den instrumentelle bredde af toppen i den observerede intensitet kan bestemmes ud fra kendskabet til denne opløsningsfunktion. Det påvises, at den instrumentelle bredde afhænger af måleproceduren, og at »fokusering«, resulterende i smalle toppe, kan opnås under visse betingelser. Ud fra de differentielle tværsnit beregnes ved hjælp af opløsningsfunktionen tværsnittene for uelastisk og elastisk neutronspredning. Endelig diskuteres valg af måleprocedure, og nogle af de vigtigste kilder til forstyrrende reflektioner omtales.

Resultaterne af målingerne og interpretationen af disse gives i kapitel III. Først omtales målinger af dispersionsrelationerne for magnoner i symmetriretninger udført over et stort temperaturområde i ferromagnetisk Tb, samt i den ferromagnetiske fase og spiralfasen i Tb–10% Ho. Den indirekte vekselvirkning afledt heraf henføres til Fermioverfladen. Ud fra målinger af bredden af toppene i den uelastisk spredte neutronintensitet som funktion af magnonbølgevektoren påvises, at magnonlevetiderne hovedsagelig er bestemt af vekselvirkningen med ledningselektronerne. Det bratte fald i bredden for små magnon-bølgevektorer skyldes sandsynligvis opsplitningen af spin-op og spin-ned Fermioverfladerne i den ferromagnetiske fase. En anomali i dispersionskurven for c-retningen i Tb–10% Ho tilskrives en kraftig vekselvirkning mellem magnoner og fononer i området, hvor magnon- og fonondispersionskurverne skærer hinanden, med resulterende blandede magnon-fonon tilstande. Endelig omtales en resonans-magnon-tilstand observeret i Tb–10% Ho. Denne tilstand opstår, fordi Ho atomernes magnetiske momenter er koblet relativt svagt til Tb-atomernes momenter.